New Journal of Physics
The open access journal at the forefront of physics

Deutsche Physikalische Gesellschaft DPG IOP Institute of Physics

PAPER • OPEN ACCESS

Irreversibility in scalar active turbulence: the role of topological defects

To cite this article: Byjesh N Radhakrishnan *et al* 2026 *New J. Phys.* **28** 034601

View the article online for updates and enhancements.

You may also like

- Characteristics of Mg/Ar ionisation chambers used as gamma-ray dosemeters in mixed neutron-photon fields
J Zoetelief, D Schlegel-Bickmann, H Schraube et al.

- Experimental and numerical assessment of two reconstructive techniques for the fragility fractures of the pelvis type Ia
Ahmed Soliman, Slawomir Kedziora, Jens Kelm et al.

- The 2022 magneto-optics roadmap
Alexey Kimel, Anatoly Zvezdin, Sangeeta Sharma et al.

This content was downloaded from IP address 85.94.226.58 on 27/02/2026 at 09:35

IOP Publishing New J. Phys. 28 (2026) 034601 https://doi.org/10.1088/1367-2630/ae44c3

New Journal of Physics
The open access journal at the forefront of physics

Deutsche Physikalische Gesellschaft DPG
IOP Institute of Physics

Published in partnership with: Deutsche Physikalische Gesellschaft and the Institute of Physics

Check for updates

PAPER

Irreversibility in scalar active turbulence: the role of topological defects

Byjesh N Radhakrishnan[1], **Francesco Serafin**[1,*], **Thomas L Schmidt and Étienne Fodor**

Department of Physics and Materials Science, University of Luxembourg, L-1511 Luxembourg, Luxembourg

[1] These authors contributed equally to this work.
[*] Author to whom any correspondence should be addressed.

E-mail: francesco.serafin@uni.lu

Keywords: irreversibility, topological defects, active turbulence

Supplementary material for this article is available online

OPEN ACCESS

RECEIVED
3 August 2025

REVISED
15 January 2026

ACCEPTED FOR PUBLICATION
11 February 2026

PUBLISHED
27 February 2026

Original Content from this work may be used under the terms of the Creative Commons Attribution 4.0 licence.

Any further distribution of this work must maintain attribution to the author(s) and the title of the work, journal citation and DOI.

Abstract

In many active systems, swimmers collectively stir the surrounding fluid to stabilize some self-sustained vortices. The resulting nonequilibrium state is often referred to as active turbulence. Although active turbulence clearly operates far from equilibrium, it can be challenging to pinpoint which emergent features primarily control the deviation from an equilibrium reversible dynamics. Here, we reveal that dynamical irreversibility essentially stems from singularities in the active stress. Specifically, considering the coupled dynamics of the swimmer density and the stream function, we demonstrate that the symmetries of vortical flows around defects determine the overall irreversibility. Our detailed analysis leads to identifying specific configurations of defect pairs as the dominant contribution to irreversibility.

1. Introduction

In active systems, each unit extracts energy from and transfers work to its surroundings [1, 2]. The violation of time-reversal symmetry (TRS) at the microscale yields nonequilibrium collective states; for instance, collective directed motion [3], motility-induced phase separation (MIPS) [4], and spatiotemporal chaotic flows referred to as *active turbulence* [5]. From a top-down perspective, continuum theories based on symmetry arguments, which are inspired by equilibrium theories [6], capture nonequilibrium states by considering additional terms breaking TRS [7–9]. In the presence of a momentum-conserving fluid, wet theories describe the coupling between the emergence of order, for instance nematics [10], and the advection of large-scale flows.

Active turbulence has attracted increasing attention due to similarities with passive turbulence, such as power-law scaling of the flow velocity fluctuations [11]. Yet, recent works have revealed that active turbulence does not require any inertia and does not feature any energy cascade [12], in contrast with its passive counterpart. Remarkably, various active systems can feature active turbulence: bacterial suspensions [13–17], swarming sperms [18], motility assays [19–22], cell monolayers [23–25] and suspensions of self-propelled colloids [23–25]. A distinct attribute of active turbulence is the sustained creation and annihilation of topological defects (TDs): these singularities correspond to disclinations in the nematic texture which are stirred by vortical flow [10, 23, 26–28]. Effective interactions between defects can be described as being mediated by the interplay between elastic distortions of the nematic texture and active flows [26, 29, 30].

Quantifying TRS breakdown is a way to measure the deviation from equilibrium [31–33]. In fact, TRS is the essential symmetry of passive dynamics [34], from which all equilibrium properties follow. In active matter, identifying the regime of weak TRS is a route towards a perturbative analysis of nonequilibrum features close to equilibrium [35–42]. For thermodynamically-consistent active models [9, 40, 43–47], quantifying TRS breakdown provides access to the amount of energy dissipated into the thermostat, which coincides with the entropy production in steady state [48, 49]. In most active models, where the

© 2026 The Author(s). Published by IOP Publishing Ltd on behalf of the Institute of Physics and Deutsche Physikalische Gesellschaft

dynamics of underlying (chemical) degrees of freedom is discarded, although measuring irreversibility underestimates dissipation, it leads to identifying near-equilibrium regimes. To this end, one can define an *informatic entropy production rate* (IEPR) by comparing the probability of forward and time-reversed trajectories [50].

To elucidate the relation between TRS breakdown and nonequilibrium patterns, it is convenient to introduce a local decomposition of IEPR [50]. For MIPS [4], this approach has revealed the essential role of nonequilibrium forces in shaping the interface between dilute and dense regions [8, 37], in line with thermodynamically consistent models [9, 45]. In a similar fashion, the decomposition of IEPR can be examined in a broad class of active hydrodynamics theories. For instance, recent works have shown how fluid flows can destabilize active phase separation, yielding a regime akin to active turbulence [51–55]. In this context, it remains to explore whether the local IEPR can be related to any striking features of the self-sustained flows.

In this paper, we examine the interplay between IEPR and TDs in a continuum model of active turbulence. Inspired by previous works [51–55], our model describes the density dynamics of swimmers immersed in a momentum-conserving fluid. Recently, In analogy with the turbulence of active nematics [12], we show that vortical flows can spontaneously form despite the absence of inertia. By analytically deriving the IEPR, we demonstrate that the dominant contribution to irreversibility stems from vortices. We also show that the IEPR is a lower bound of the total dissipation derived from linear irreversible thermodynamics (LITs). Finally, we propose a mapping between the shear stress, which stirs the fluid, and an effective nematic field. Such a mapping leads to delineating singularities in the density profile which shape the surrounding vortices. In all, our results reveal how the symmetries of vertical flows, set by TDs, determine the spatial distribution of IEPR.

The paper is structured as follows. In section 2, we start by introducing our continuum theory, and reviewing the associated phenomenology: laminar, vortex, and turbulent states. We then show that the zeros of density gradients correspond to nematic-like singularities, and numerically evaluate the corresponding defect statistics. In section 3, we explicitly relate the IEPR to the vorticity, and provide a numerical quantification in the noiseless regime. We also find a generic relation between the IEPR and the total dissipation. We find that in steady state the IEPR is a lower bound to the total EPR. Finally, by computing the vorticity around defects, we examine in detail how the spatial distribution of IEPR is determined by the symmetries of defects.

2. Turbulence in active model H

In this section, we present the dynamics of Active Model H (AMH) [51] in the absence of inertia. This dynamics couples two fields: (i) a conserved scalar field, representing the local density of active swimmers, and (ii) a non-conserved scalar field corresponding to the stream function of the surrounding fluid flow. We characterize the emergence of three main states: laminar flow, vortex array, and turbulence. We discuss the spontaneous formation of TDs by analyzing the profile of density gradients.

2.1. Coupled dynamics of density and stream function

Inspired by previous works [51, 52], we start by considering the dynamics of the local density of active swimmers $\phi(\boldsymbol{r},t)$ coupled to the velocity $\boldsymbol{v}(\boldsymbol{r},t)$ of a momentum-conserving fluid

$$\dot{\phi}+\boldsymbol{v}\cdot\nabla\phi=-\nabla\cdot\boldsymbol{J},\quad \boldsymbol{J}=-M\nabla\frac{\delta\mathcal{F}}{\delta\phi}+\sqrt{2MT}\boldsymbol{\Lambda}_{\phi}, \tag{1}$$

where M is the mobility, and T the temperature (we use units in which $k_B=1$). We set $M=1$ in the following. The noise $\boldsymbol{\Lambda}$ is Gaussian with zero mean and correlations given by

$$\langle\Lambda_{\phi,\alpha}(\boldsymbol{r},t)\,\Lambda_{\phi,\beta}(\boldsymbol{r}',t')\rangle=\delta_{\alpha\beta}\delta(\boldsymbol{r}-\boldsymbol{r}')\,\delta(t-t'). \tag{2}$$

We take for the free-energy functional $\mathcal{F}$ a form analogous to a Landau–Ginzburg expansion:

$$\mathcal{F}[\phi]=\int\left[\frac{\kappa}{2}(\nabla\phi)^2+g(\phi)\right]\mathrm{d}\boldsymbol{r},\quad g(\phi)=\frac{a}{2}\phi^2+\frac{b}{4}\phi^4, \tag{3}$$

where (κ,a,b) are parameters. A phase separation emerges for $a<0$ and $b,\kappa>0$ [7, 56, 57]. The density dynamics in equation (1) must be supplemented with the Navier–Stokes equation for the velocity dynamics:

$$\rho(\partial_t v_\alpha+v_\beta\partial_\beta v_\alpha)=\eta\nabla^2 v_\alpha-\partial_\alpha p+\partial_\beta\left(\Sigma^P_{\alpha\beta}+\Sigma^A_{\alpha\beta}+\sqrt{2\eta T}\Gamma_{\alpha\beta}\right), \tag{4}$$

where ρ is the fluid's density, $p(\boldsymbol{r},t)$ the pressure field, and η the fluid's viscosity. Summation over repeated indices is assumed throughout the paper. The fluid's density obeys the continuity equation $\partial_t\rho+\partial_\beta(\rho v_\beta)=0$. Here, $\Gamma_{\alpha\beta}$ is a Gaussian noise field with zero mean and correlations given by [58]

$$\langle\Gamma_{\alpha\beta}(\boldsymbol{r},t)\Gamma_{\mu\nu}(\boldsymbol{r}',t')\rangle=(\delta_{\alpha\mu}\delta_{\beta\nu}+\delta_{\alpha\nu}\delta_{\beta\mu})\,\delta(\boldsymbol{r}-\boldsymbol{r}')\,\delta(t-t')\,. \tag{5}$$

The passive and active contributions to the deviatoric stress, respectively $\Sigma^P_{\alpha\beta}$ and $\Sigma^A_{\alpha\beta}$, read

$$\Sigma^P_{\alpha\beta}=-\kappa\left[(\partial_\alpha\phi)(\partial_\beta\phi)-\frac{1}{2}|\nabla\phi|^2\delta_{\alpha\beta}\right],\quad \Sigma^A_{\alpha\beta}=-\zeta\left[(\partial_\alpha\phi)(\partial_\beta\phi)-\frac{1}{2}|\nabla\phi|^2\delta_{\alpha\beta}\right], \tag{6}$$

where ζ is the activity parameter [51]. In passive systems, the expression of $\Sigma^P_{\alpha\beta}$ can be derived from the free-energy functional $\mathcal{F}[\phi]$ [59]. To the lowest order in powers of ϕ and its gradient, the term $\partial_\alpha\phi\partial_\beta\phi-\frac{1}{2}|\nabla\phi|^2\delta_{\alpha\beta}$ is the only traceless symmetric tensor that can be constructed, so that we assume that $\Sigma^A_{\alpha\beta}$ must be proportional to it. The sign of ζ distinguishes the cases of contractile ($\zeta<0$) and extensile ($\zeta>0$) swimmers. The active stress is the only source of activity in the dynamics. Beyond fluid-like systems, recently it was proposed that the active stress of AMH could play a role in active tissues by mediating the coupling between a scalar concentration of proteins and the mechanical stresses in the tissue [60–62].

In the following, we assume that the system is overdamped, and neglect the inertial term in equation (4). The fluid's density decouples from the other fields. We further assume that the fluid is incompressible and we neglect inertial forces, yielding the Stokes equation:

$$\eta\nabla^2 v_\alpha=\partial_\alpha p-\partial_\beta\left(\Sigma^P_{\alpha\beta}+\Sigma^A_{\alpha\beta}+\sqrt{2\eta T}\,\Gamma_{\alpha\beta}\right),\quad \nabla\cdot\boldsymbol{v}=0\,, \tag{7}$$

where

$$f^A{}_\alpha=\partial_\beta\Sigma^A_{\alpha\beta} \tag{8}$$

is the active force and $f_\alpha=\partial_\beta(\Sigma^P_{\alpha\beta}+\Sigma^A_{\alpha\beta})$ is the total force. To eliminate the pressure contribution in equation (7), we define the stream function $\psi(\boldsymbol{r},t)$ as

$$v_x=\partial_y\psi\,,\quad v_y=-\partial_x\psi\,, \tag{9}$$

or, $v_\alpha=\epsilon_{\alpha\beta}\partial_\beta\psi$ (where $\epsilon_{\alpha\beta}=-\epsilon_{\beta\alpha}$, $\epsilon_{xy}=+1$ is the Levi–Civita symbol in 2 dimensions). By taking the curl of equation (7) and using equation (9), the Stokes equation reduces to

$$\eta\nabla^4\psi=(\kappa+\zeta)\left[(\partial_x\phi)\nabla^2(\partial_y\phi)-(\partial_y\phi)\nabla^2(\partial_x\phi)\right]-\sqrt{2\eta T}\,\nabla^2\Lambda_\psi\,, \tag{10}$$

where Λ_ψ is a scalar Gaussian noise with zero mean and correlations given by (appendix A)

$$\langle\Lambda_\psi(\boldsymbol{r},t)\Lambda_\psi(\boldsymbol{r}',t')\rangle=\delta(\boldsymbol{r}-\boldsymbol{r}')\,\delta(t-t')\,. \tag{11}$$

In equation (10), the vorticity $\omega=-\nabla^2\psi$ is sourced by a combination of passive and active stresses. The latter stir the system out of equilibrium and can generate spatiotemporal chaotic flow [51]. In what follows, we analyze the field dynamics of AMH as governed by equations (1) and (10).

2.2. Laminar, vortex and turbulent states

We numerically simulate AMH (equations (1) and (10)) with the integration scheme detailed in appendix B. The parameters are fixed to $-a=b=0.1$, $\kappa=0.1$, and $\eta=1.67$, and we vary the activity parameter $\zeta<0$, namely, considering contractile activity. The extensile case ($\zeta>0$) does not have turbulent phases, so it is not relevant for our study which focuses on the turbulent, defect-rich phase.

For small activity ζ, we report a full phase separation of the density ϕ between dilute ($\phi=-1$) and dense ($\phi=1$); the stream function ψ forms either a laminar state (figure 1(a)) or a vortex state (figure 1(b)). The profiles of (ϕ,ψ) have a wavelength of the order to the system size, L. The flow speed increases with ζ, particularly between domains of ϕ where the flow is concentrated, which leads to destabilizing the laminar flow and favors patterns made of vortices. At even larger ζ, the vortex pattern

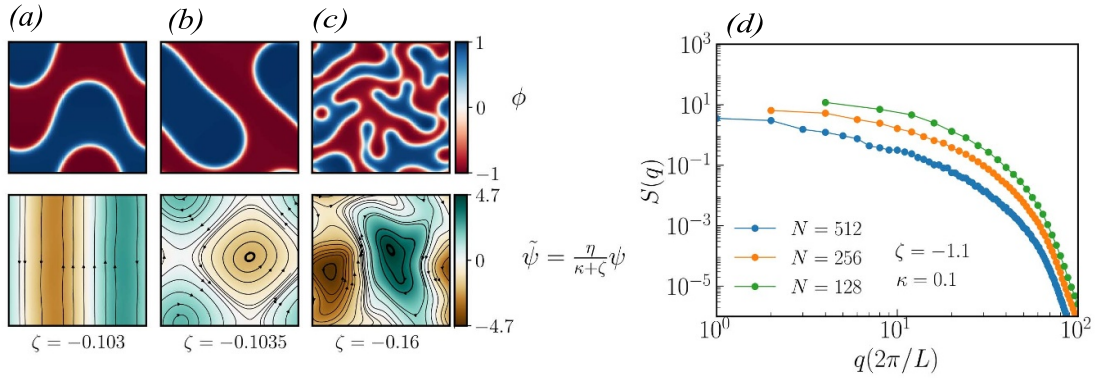

Figure 1. For Active Model H (equations (1) and (10)), the swimmer density ϕ (top) and the scaled stream function $\tilde{\psi} = \frac{\eta}{\zeta+\kappa}\psi$ (bottom) feature three possible steady states for different levels of activity ζ: (a) laminar flow, (b) vortex, and (c) spatio-temporal chaos (referred to as the turbulent state). The black lines with arrows show the velocity field lines. Parameters $-a = b = 0.1$, $\kappa = 0.1$, and $\eta = 1.67$. (d) Velocity spectrum $S(q)$ (equation (16)) as a function of wavenumber q (scaled by the largest system size) for $\zeta = -1.1$.

becomes unstable, and the system enters a self-sustained dynamical steady state (figure 1(c)), analogous to *active turbulence* [51, 52]. In the turbulent state, we measure the velocity spectrum $S(q)$ defined by [12]

$$\langle \boldsymbol{v}^2 \rangle = \int q \, \langle |\boldsymbol{v}_{\boldsymbol{q}}|^2 \rangle \, \mathrm{d}q = \int S(q) \, \mathrm{d}q, \tag{12}$$

where $q = |\boldsymbol{q}|$, and $\boldsymbol{v}_{\boldsymbol{q}}$ is the spatial Fourier transform of $\boldsymbol{v}(\boldsymbol{r})$. We observe that $S(q)$ decays monotonically with q (figure 1(d)). For AMH with inertia, the scaling $S(q) \sim q^{-7/5}$ has been reported in the turbulent regime [54]. Here, we cannot infer any specific power-law scalings from our simulations. Numerical measurements for a broader span of q might reveal such scalings. We defer this analysis to future work.

2.3. Topological defects

The turbulent state is associated with the sustained creation and annihilation of TDs. We discuss below how these defects can be detected and analyzed as singularities in the profile of the active stress $\Sigma^A_{\alpha\beta}$ (equation (6)).

We construct from $\Sigma^A_{\alpha\beta}$ a symmetric traceless tensor $Q_{\alpha\beta} = \zeta^{-1}\Sigma^A_{\alpha\beta}$ analogous to the nematic order parameter of liquid crystals in 2 dimensions [63]:

$$\mathbb{Q} = \begin{pmatrix} Q_{11} & Q_{12} \\ Q_{12} & -Q_{11} \end{pmatrix}, \tag{13}$$

where

$$Q_{11} = -\frac{1}{2}\left[(\partial_x\phi)^2 - (\partial_y\phi)^2\right], \quad Q_{12} = -(\partial_x\phi)(\partial_y\phi). \tag{14}$$

Our interpretation of active stress as a nematic field differs from [10], where the nematic field was instead associated with a deformation tensor. We interpret the *orientation* of the principal axes of $\mathbb{Q}$ in analogy with a nematic director. The principal axes are obtained from the eigenvectors $\mathbf{v}_\pm$ of $\mathbb{Q}$ by identifying $\mathbf{v}_\pm \sim -\mathbf{v}_\pm$ (appendix C). This identification defines a local orientation, which we interpret as the analog of a nematic director field:

$$\mathbf{v}_+ = \left[(\partial_x\phi)/(\partial_y\phi), 1\right] \equiv |\mathbf{v}_+|\,[\cos\theta_N, \sin\theta_N], \quad \theta_N = \tan^{-1}\frac{\partial_y\phi}{\partial_x\phi}. \tag{15}$$

The angle θ_N represents the orientation of the principal axes of stress if we identify $\theta_N \sim \theta_N + \pi$. In fact, we deduce from equation (15) that θ_N coincides locally with the direction θ of $\nabla\phi$. Importantly, while θ winds from 0 to 2π (e.g. $\nabla\phi$ and $-\nabla\phi$ are distinct vectors), the nematic-like orientation is defined modulo π, since $\mathbf{v}_+$ and $-\mathbf{v}_+$ represent the same orientation. Therefore, the singularities of the nematic tensor $\mathbb{Q}$, namely TDs where θ_N is undefined, are located at the critical points of the field ϕ, namely where $|\nabla\phi| = 0$ (figure 2). The orientation θ_N winds by multiples of π around the point-singularities of $\mathbb{Q}$, so the topological charge is quantized in half-integer multiples: $\frac{1}{2\pi}\oint_\gamma \nabla\theta_N \cdot \mathrm{d}\boldsymbol{\ell} = \frac{s}{2}$, $(s = \pm1, \pm2, \ldots)$

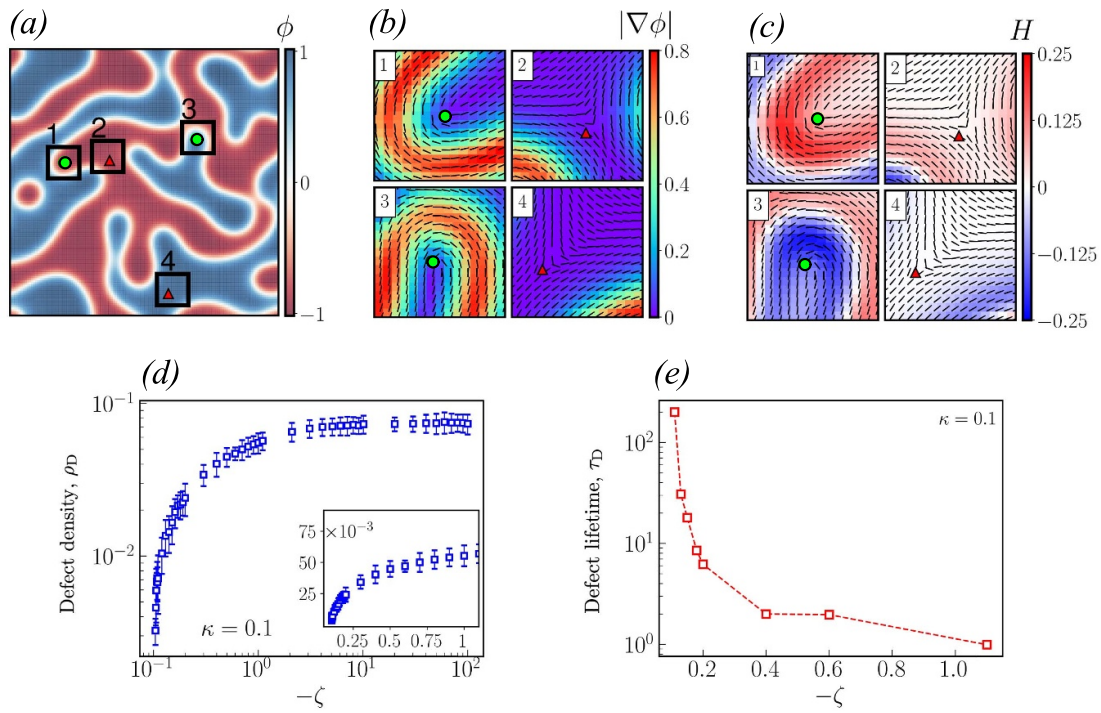

Figure 2. (a) Density field ϕ in the turbulent state ($\zeta = -0.16$). The markers indicate the locations of $+\frac{1}{2}$ (green circles) and $-\frac{1}{2}$ (red triangles) topological defects. Panels (b), (c): zoomed–in view of the four squares marked in panel (a): comparison between the location of the defects, the nematic director field (black lines) along with (b) the density gradient $|\nabla\phi|$ and (c) the local curvature H. (d) Density of defects $\rho_D = \langle N_D \rangle / L^2$, where $\langle N_D \rangle$ is the defect number averaged over time and realizations, and (e) defect lifetime τ_D, defined as the average time between pair creation and annihilation, as functions of the activity parameter ζ. Parameters $-a = b = 0.1$, $\kappa = 0.1$, and $\eta = 1.67$.

for every loop γ enclosing a defect. This connection provides a convenient description to identify and track TDs. In appendix C, we show that the amplitude S of the $Q-$tensor reads

$$S = \sqrt{Q_{11}^2 + Q_{12}^2} = \frac{1}{2}|\nabla\phi|^2 \tag{16}$$

which vanishes at the critical points of ϕ, namely at the center of the TDs, as expected. In active nematics, the core radius is the typical length scale in which S varies from 1 to 0; however, here S is not an order parameter field. The core is set by the typical spatial variation of $|\nabla\phi|$ around the critical points of ϕ, see for instance figure 2(b). We refer the reader to appendix F for further discussion on the core size.

In numerical simulations, we compare the orientation of the nematic field $\mathbb{Q}$ and that of $\nabla\phi$ (figures 2(a) and (b)). The locations of TDs, with charge $\pm\frac{1}{2}$, indeed coincide with the zeros of $\nabla\phi$. In fact, $+\frac{1}{2}$ defects are typically located close to interfaces between dense and dilute phases, whereas $-\frac{1}{2}$ defects are immersed in the bulk phases. It is insightful to interpret the field $\phi(x,y)$ as the height of a topographic surface in the Monge parametrization: this interpretation provides a direct correspondence between the location defects (where $\nabla\phi$ vanishes) and the local curvature H associated with ϕ (appendix C). In fact, the $+\frac{1}{2}$ defects are located at the maxima and minima of curvature, whereas $-\frac{1}{2}$ defects are located at the saddle points where $H = 0$ (figure 2(c)). Evaluating the density ρ_D (figure 2(d)) and lifetime τ_L (figure 2(e)) of defects, we find that ρ_D increase monotonically and reaches a plateau at large ζ, whereas τ_D decreases monotonically. These measurements support the fact that the reduced lifetime stems from the increase in defect motility at high activity.

In short, the analogy between shear stress and nematic tensor means that singularities in the stress profile must have $\pm\frac{1}{2}$ charges. Moreover, such defects can actually be detected simply by analyzing the profile of swimmer density ϕ, without any information on the surrounding flow. In what follows, to analyze the turbulent phase of AMH, we use three equivalent levels of description: (i) the density of microswimmers measured by the scalar field ϕ (figure 2(a)), (ii) the stresses (passive and active) represented by the nematic order parameter $\mathbb{Q}$ (equation (13) and figure 3(a)), and (iii) the forces (passive and active, see equation (8)) which are proportional to $\nabla \cdot \mathbb{Q}$ (figure 3(b)). The forces are the sources of the active flows (equation (7)) which stir the TDs.

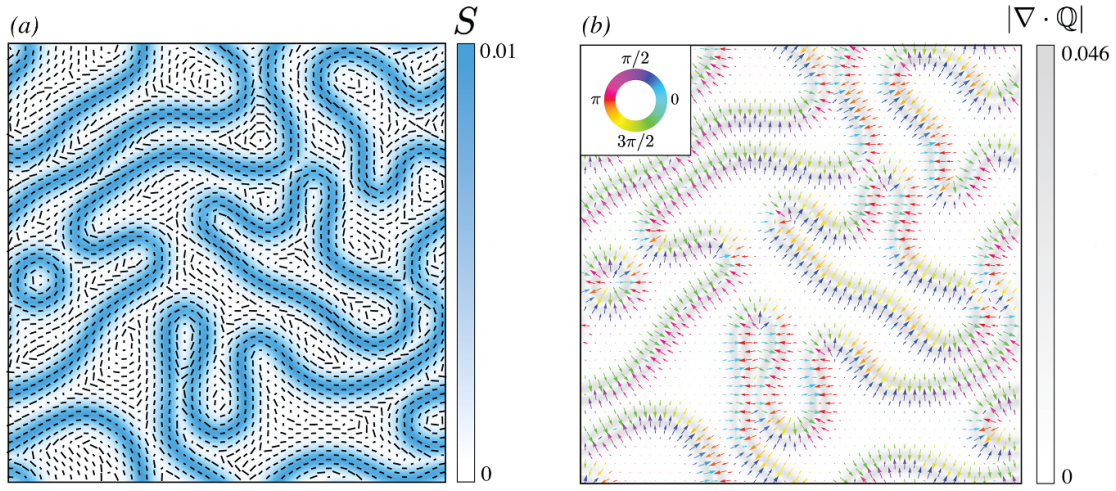

Figure 3. (a) Nematic order parameter $\mathbb{Q}$ (equations (13) and (14)) extracted from the density field ϕ in figure 2(a). The black lines correspond to the director field representing the nematic orientation θ_N (equation (15)). The blue colorscale corresponds to the amplitude S of $\mathbb{Q}$ (equation (16)) that is maximal at interfaces between dense and dilute regions (figure 2(a)). (b) Total force field is proportional to $\nabla \cdot \mathbb{Q}$ (equation (8)). The gray colorscale corresponds to the amplitude of the total force that is localized at the interfaces. The colored arrows refer to the orientation of the force vectors, see inset.

3. Quantifying irreversibility from vorticity and TDs

In this section, we propose a quantification of TRS, called IEPR, and study its features in the turbulent state. We provide a local measure of IEPR and examine its relations with TDs. We successfully compare our predictions for the local IEPR with simulations in the vicinity of defects.

3.1. IEPR as a measure of irreversibility

Following standard tools of stochastic thermodynamics [31, 48, 50], the IEPR $\dot{\mathcal{S}}$ is defined as

$$\dot{\mathcal{S}} = \lim_{\tau\to\infty} \frac{1}{\tau} \ln \frac{\mathcal{P}\left(\{\boldsymbol{J},\psi\}_0^\tau\right)}{\mathcal{P}^R\left(\{\boldsymbol{J},\psi\}_0^\tau\right)} \geqslant 0, \tag{17}$$

where $\mathcal{P}(\{\boldsymbol{J},\psi\}_0^\tau)$ is the probability of a given trajectory within the time interval $0 \leqslant t \leqslant \tau$, and $\mathcal{P}^R(\{\boldsymbol{J},\psi\}_0^\tau)$ the probability of its time-reversed image. In general, the IEPR depends on the strength of fluctuations. In what follows, we focus on the regime of vanishing noise ($T \to 0$) which gives insight into how deterministic dynamical patterns contribute to irreversibility [8, 36]. Using field theoretical methods [64–66], we calculate the dominant contribution to IEPR in steady state (appendix D):

$$T\dot{\mathcal{S}} = \int \dot{\sigma}\left(\boldsymbol{r}\right) \mathrm{d}\boldsymbol{r}, \quad \dot{\sigma}\left(\boldsymbol{r}\right) = \frac{\eta\zeta}{\kappa+\zeta}\langle\omega^2\rangle \geqslant 0, \tag{18}$$

where $\omega = -\nabla^2\psi$ is the local vorticity, and $\langle\cdot\rangle$ is an average over time and realizations (under the assumption of ergodicity). Therefore, the IEPR is proportional to the enstrophy $\int\langle\omega^2\rangle \mathrm{d}\boldsymbol{r}$ [67], and we have defined the local density of IEPR $\dot{\sigma}(\boldsymbol{r})$. The IEPR vanishes at zero activity ($\zeta = 0$), as expected: since activity is the only source of stirring in this system, removing it stops all vortical motions. Note that the regime of zero viscosity is a singular limit, since the assumption of negligible inertia underlying the Stokes equation (equation (7)) breaks down.

The local IEPR can also be written in terms of the curl of the velocity field, since $\omega^2 = (\nabla \times \boldsymbol{v})^2$:

$$\dot{\sigma}\left(\boldsymbol{r}\right) = \frac{\eta\zeta}{\kappa+\zeta}\langle(\nabla\times\boldsymbol{v})^2\rangle = \frac{\eta\zeta}{\kappa+\zeta}\langle\left(\nabla^2\psi\right)^2\rangle. \tag{19}$$

The non-negativity of the local IEPR $\dot{\sigma}(\boldsymbol{r})$ may not be immediately obvious from equation (18). For $-\kappa \leqslant \zeta \leqslant 0$, although the term $\zeta/(\kappa+\zeta)$ is negative, the steady state is fully phase-separated state without any flow, so $\dot{\sigma}(\boldsymbol{r})$ vanishes. Note that $\dot{\sigma}$ is invariant with respect to a gauge transformation $\psi \to \psi + c$ for an arbitrary constant c, as required by gauge invariance. In the laminar state $\dot{\mathcal{S}} = 0$, since there is no vorticity ($\nabla^2\psi = 0$), whereas in the vortex state $\dot{\mathcal{S}}$ does not vanish. In the turbulent state, $\dot{\mathcal{S}}$ first increases rapidly with ζ, and then saturates at large ζ. This observation is robust to variation in (b,η) (figure 4).

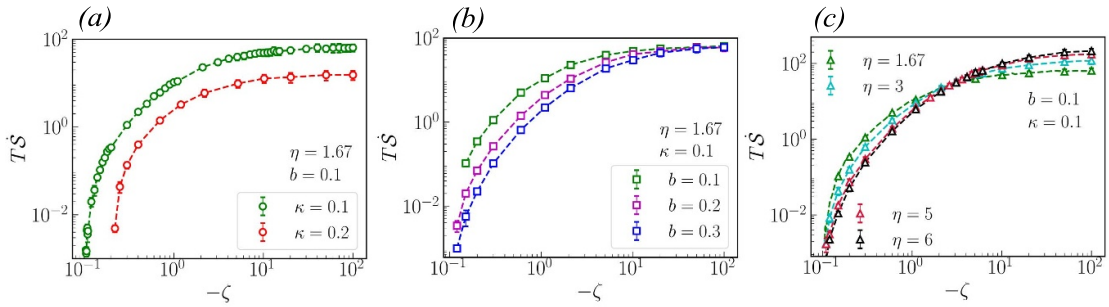

Figure 4. Informatic entropy production rate (IEPR) (equation (18)) in steady state as a function of activity ζ, when changing (a) the cost at density gradients κ, (b) the nonlinear free-energy coefficient b, and (c) the viscosity η. Same parameters as in figure 1.

In short, equation (18) shows that the local IEPR can be extracted from local measurements of the flow field (namely, either $\boldsymbol{v}$, ω or ψ), and that the symmetries of the flow field determine the distribution of IEPR in space. Specifically, the regions of high vorticity ω are associated with high IEPR $\dot{\sigma}$. This relation is relevant for estimating the local irreversibility of scalar active matter in experiments where the local flow can be inferred by visual techniques, such as PIV methods [16, 68].

3.2. Linear irreversible thermodynamics

Some active field theories are postulated from symmetry arguments without any energetic arguments [69], while others are based on the definition of the total dissipation [1, 70]. In many hydrodynamic theories, the dissipation can be written in terms of the products of some thermodynamic forces and currents; LIT enforces linear relations between these forces and currents [71]. To account for the continuous energy injection fueling activity in AMH, we must add to (ϕ, ψ) the dynamics of some reactant fields n. Inspired by [9], we demonstrate how to embed the dynamics of AMH (equations (1) and (10)) in the extended field space (ϕ, ψ, n) within the framework of LIT [71]. Such an embedding provides a route to relating the IEPR (equation (17)) with the total dissipation.

By analogy with active gel theories [70], we assume that our system is in contact with some reservoirs of product and reactant molecules at a fixed chemical potential difference $\Delta\mu$. Molecules undergo chemical reactions at a constant rate r, and such reactions generate nonequilibrium mechanical forces that sustain the activity of swimmers. Therefore, to leading order, we assume that the activity parameter ζ (equation (6)) is proportional to $\Delta\mu$, so we express the active stress $\Sigma^A_{\alpha\beta}$ as follows:

$$\Sigma^A_{\alpha\beta} = -\Delta\mu\,\tilde{\Sigma}^A_{\alpha\beta}\,. \tag{20}$$

At small Reynolds number, we write down the Stokes equation (equation (7)) as

$$\partial_\beta \Sigma^{\mathrm{tot}}_{\alpha\beta} = 0, \tag{21}$$

where

$$\begin{aligned} \Sigma^{\mathrm{tot}}_{\alpha\beta} &= 2\eta v_{\alpha\beta} + \Sigma^{P,\mathrm{tot}}_{\alpha\beta} - \Delta\mu\tilde{\Sigma}^A_{\alpha\beta}, \\ \Sigma^{P,\mathrm{tot}}_{\alpha\beta} &= \Sigma^P_{\alpha\beta} - p\delta_{\alpha\beta}, \\ 2v_{\alpha\beta} &= \partial_\alpha v_\beta + \partial_\beta v_\alpha, \end{aligned} \tag{22}$$

where $v_{\alpha\beta}$ is the strain rate tensor, and $\Sigma^{P,\mathrm{tot}}_{\alpha\beta}$ includes the pressure p. We then rewrite the noiseless dynamics of AMH (equations (1) and (21)) in terms of the following thermodynamic forces $\mathbb{X}$ and currents $\mathbb{J}$:

$$\mathbb{X} = \left(-\partial_\alpha \frac{\delta\mathcal{F}}{\delta\phi}, \Sigma^{\mathrm{tot}}_{\alpha\beta} - \Sigma^{P,\mathrm{tot}}_{\alpha\beta}, \Delta\mu\right)^{\mathrm{T}}, \quad \mathbb{J} = (J_\alpha, v_{\alpha\beta}, r)^{\mathrm{T}}, \tag{23}$$

that are linearly related through the Onsager matrix $\mathbb{L}$:

$$\mathbb{J} = \mathbb{L}\cdot\mathbb{X}, \quad \mathbb{L} = \begin{pmatrix} M & 0 & 0 \\ 0 & (2\eta)^{-1} & (2\eta)^{-1}\tilde{\Sigma}^A_{\alpha\beta} \\ 0 & (2\eta)^{-1}\tilde{\Sigma}^A_{\alpha\beta} & c_r \end{pmatrix}. \tag{24}$$

In writing equation (24), we have introduced the kinetic coefficient c_r, and we have used that $\mathbb{L}$ must be symmetric for dissipative fluxes and forces [66]. The stability of the dynamics enforces that $\mathbb{L}$ is positive semi-definite [71], which provides an explicit constraint on c_r as

$$\int (\det \mathbb{L})\, \mathrm{d}\boldsymbol{r} = \frac{M}{2\eta} \int \left(c_r - \frac{1}{2\eta} \tilde{\Sigma}^A_{\alpha\beta} \tilde{\Sigma}^A_{\alpha\beta} \right) \mathrm{d}\boldsymbol{r} \geqslant 0. \tag{25}$$

As a result, embedding AMH (equations (1) and (21)) into the extended field space (ϕ, ψ, n) within LIT (equation (24)) amounts to writing the local chemical rate r as a linear combination of the fluid's velocity $\boldsymbol{v}$ and the auxiliary field $\tilde{\Sigma}^A_{\alpha\beta}$:

$$r = c_r \Delta\mu + v_{\alpha\beta} \tilde{\Sigma}^A_{\alpha\beta} - \frac{\Delta\mu}{2\eta} \tilde{\Sigma}^A_{\alpha\beta} \tilde{\Sigma}^A_{\alpha\beta}, \tag{26}$$

where we have used equation (24). Note that since the active stress is proportional to $\Delta\mu$ and the latter is constant in space and time, the original AMH dynamics for the swimmer concentration ϕ and the stream function ψ remains unchanged.

The rate of energy dissipated by the system can be written as ([71], appendix E)

$$T\dot{\mathcal{S}}_{\mathrm{tot}} = \int (\mathbb{J} \cdot \mathbb{X})\, \mathrm{d}\boldsymbol{r} = -\frac{\mathrm{d}\mathcal{F}}{\mathrm{d}t} + \int (r\Delta\mu)\, \mathrm{d}\boldsymbol{r} \geqslant 0. \tag{27}$$

Such a linear relation between dissipation, forces, and fluxes holds even in the presence of fluctuations [9]. The term $-\mathrm{d}\mathcal{F}/\mathrm{d}t$ in equation (27) accounts for the transient relaxation (and vanishes in steady state), whereas the term $r\Delta\mu$ describes how the profiles (ϕ, ψ) affect dissipation. For homogeneous profiles (namely, when $\tilde{\Sigma}^A_{\alpha\beta} = 0$), the IEPR $\dot{\mathcal{S}}$ vanishes (equation (18)), whereas substituting the definition of r (equation (26)) into equation (27) yields a positive dissipation rate $\dot{\mathcal{S}}_{\mathrm{tot}} \sim c_r \Delta\mu^2$. In other words, even in the absence of any patterns in (ϕ, ψ), there is a positive dissipation due to the underlying chemical reactions.

For arbitrary profiles (ϕ, ψ), substituting the definition of r (equation (26)) into equation (27), we identify two contributions to the steady-state dissipation $T\dot{\mathcal{S}}^{(\mathrm{ss})}_{\mathrm{tot}}$:

$$\dot{\mathcal{S}}^{(\mathrm{ss})}_{\mathrm{tot}} = \frac{(2\eta)^4 \Delta\mu^2}{M} \int (\det \mathbb{L})\, \mathrm{d}\boldsymbol{r} - \int v_{\alpha\beta} \Sigma^A_{\alpha\beta} \mathrm{d}\boldsymbol{r}. \tag{28}$$

We demonstrate in appendix E that the second term in equation (28) coincides with the IEPR $T\dot{\mathcal{S}}$ (equation (18)). In conclusion, $\dot{\mathcal{S}}^{(\mathrm{ss})}_{\mathrm{tot}}$ can be expressed in terms of $\dot{\mathcal{S}}$ as

$$\dot{\mathcal{S}}^{(\mathrm{ss})}_{\mathrm{tot}} = \frac{(2\eta)^4 \Delta\mu^2}{MT} \int (\det \mathbb{L})\, \mathrm{d}\boldsymbol{r} + \dot{\mathcal{S}}. \tag{29}$$

Therefore, equation (29) provides an explicit relation between the IEPR of AMH and the steady-state dissipation in the extended hydrodynamic theory. Combining equations (25) and (29), we deduce that the IEPR gives a lower bound on the total dissipation:

$$\dot{\mathcal{S}}^{(\mathrm{ss})}_{\mathrm{tot}} \geqslant \dot{\mathcal{S}} \geqslant 0. \tag{30}$$

Defining the chemical concentration n in terms of the chemical rate $r = \partial_t n$, the total dissipation $T\dot{\mathcal{S}}_{\mathrm{tot}}$ measures the irreversibility of the trajectories (ϕ, ψ, n) [9]. In contrast, $\dot{\mathcal{S}}$ only accounts for the irreversibility of (ϕ, ψ), so it provides only a partial estimation of the total dissipation. In short, the bound in equation (30) illustrates how irreversibility decreases when considering a reduced set of dynamical fields [72].

3.3. Local measurement of irreversibility: the role of TDs

In the turbulent state, the local IEPR $\dot{\sigma}$ fluctuates in the form of sharply localized regions that continuously appear and disappear in time; we refer the reader to the supplementary video. We report in figure 5(a) a typical instantaneous configuration, where the field $\dot{\sigma}$ is directly evaluated from ψ (equation (19)), showing that $\dot{\sigma}$ is typically larger at interfaces (between small- and large-ϕ regions) than in the bulks, and also higher in regions of large vorticity. We observe two necessary conditions for regions of high IEPR to emerge: (i) the interfaces form S-shaped meandering curves, and (ii) the curved interfaces enclose pairs of $+\frac{1}{2}$ TDs which are oriented perpendicular to the line connecting them (red

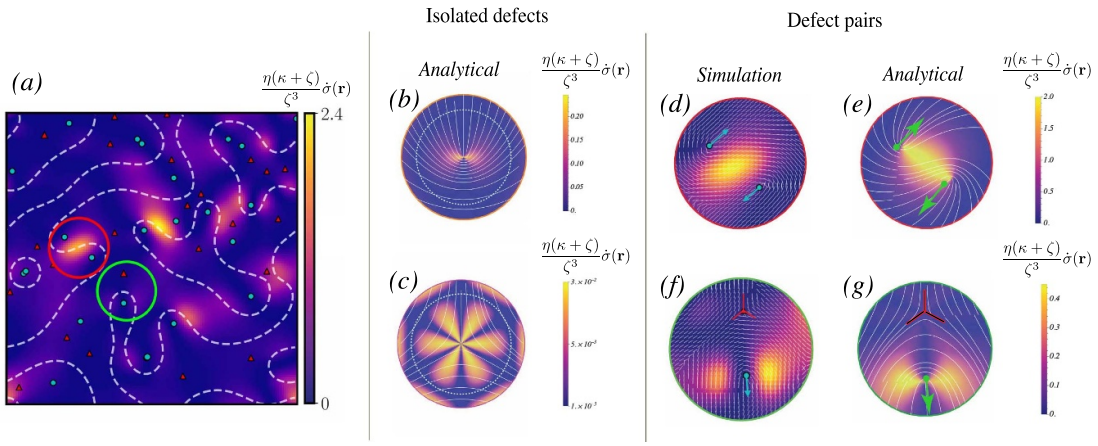

Figure 5. (a) Spatial distribution of the local IEPR $\dot{\sigma}$ (equation (19)) extracted from the same turbulent state as in figures 1(c) and 2(a). The white dashed lines represent the phase boundary $\phi = 0$. The green dots and red triangles respectively refer to $+\frac{1}{2}$ and $-\frac{1}{2}$ topological defects. (b), (c) Analytic predictions of $\dot{\sigma}$ around isolated topological defects (equation (32)) of charge $+\frac{1}{2}$ (panel (b)) and $-\frac{1}{2}$ (panel (c)). White lines refer to the nematic orientation. (d)–(g) Comparison between simulations and analytical predictions for defect pairs. A pair with charges $(+\frac{1}{2}, +\frac{1}{2})$ (d), (e) and a pair with charges $(+\frac{1}{2}, -\frac{1}{2})$ (f), (g) marked respectively with red and green circles in panel (a). We numerically evaluate the relative angle Φ and the distance d between defects (section 3.3.2). White lines refer to the nematic orientation.

circle in figures 5(a), (d) and (e)). In general, other configurations of paired TDs can produce a high IEPR locally: in a pair of $+\frac{1}{2}$ and $-\frac{1}{2}$ TDs, $\dot{\sigma}$ is locally higher close to the $+\frac{1}{2}$ defect (figure 5(f)).

In what follows, we provide analytical predictions that reproduce the IEPR profiles observed in the simulations, and argue that such profiles can be rationalized in terms of the symmetries of the TDs in the nematic field Q (equation (13)). To this end, we examine *idealized* TDs by considering either isolated TDs of charge $+\frac{1}{2}$ and $-\frac{1}{2}$ (section 3.3.1), or pairs of TDs obtained by superposing the orientation fields of two isolated defects (section 3.3.2).

3.3.1. Isolated defects

We predict analytically the intensity and the spatial symmetries of the local IEPR $\dot{\sigma}$ around isolated defects using equation (19). The flow field around isolated defects can be found analytically by assuming that (i) the amplitude of the nematic $Q-$tensor is constant, and (ii) the density field ϕ, which determines the local stress (equation (6)), relaxes faster than the stream function ψ, which determines the local flow. The stream function ψ associated with the flow field $\boldsymbol{v}$ of an isolated defect was derived in [73]. Using polar coordinates $\boldsymbol{r} = (r, \varphi)$ centered at the defect core, the solution can be written as $\psi = \bar{\psi} + \psi_0$, where

$$\bar{\psi}_{+\frac{1}{2}}(\boldsymbol{r}) = \frac{\zeta}{12\eta} r(3R - 2r)\sin\varphi\,, \quad \bar{\psi}_{-\frac{1}{2}}(\boldsymbol{r}) = \frac{\zeta}{240\eta R} r^2(5r - 8R)\sin 3\varphi\,, \tag{31}$$

and the term $\psi_0 = (a_1 r + b_1 r^3)\sin\varphi$ is a solution to the homogeneous the Stokes equation, with (a_1, b_1) being fixed by the boundary conditions. Following [73], we assume that there is a disc of radius R centered at the isolated defect which does not contain other defects. We impose vanishing radial flux through the disc's boundary ($v_r(R, \varphi) = 0$), and force-balance tangentially to the boundary: $v_\varphi(R, \varphi) = -\xi \Sigma^A_{r\varphi}$ where $\xi \sim \eta h$ and h is the thickness of the boundary layer between neighboring defects [73]. The full solution then reads

$$\psi_{+\frac{1}{2}}(\boldsymbol{r}) = \frac{\zeta}{2\eta}\left[\frac{1}{2}\left(\frac{R}{3} + \frac{\eta}{\xi}\right) r - \frac{1}{3} r^2 + \frac{1}{2}\left(\frac{R}{3} - \frac{\eta}{\xi}\right) r^3\right] \sin\varphi\,, \tag{32a}$$

$$\psi_{-\frac{1}{2}}(\boldsymbol{r}) = -\frac{\zeta}{2\eta} \frac{r^2\left(2r^3(15\eta + \xi R) - rR^2(\xi R + 30\eta) + 4\xi R^4\right)}{60\xi R^4} \sin(3\varphi)\,. \tag{32b}$$

Substituting the profiles equation (32) into the expression of the local IEPR (equation (18)), we deduce

$$T\dot{\sigma}_{+\frac{1}{2}}(\boldsymbol{r}) = \frac{\zeta^3}{\eta(\zeta + \kappa)}\left[\frac{1}{4} + \left(\frac{\eta}{R\xi} - \frac{1}{3}\right)\frac{r}{R}\right]^2 \sin^2\varphi\,, \tag{33a}$$

$$T\dot{\sigma}_{-\frac{1}{2}}(\boldsymbol{r}) = \frac{\zeta^3}{\eta(\zeta+\kappa)}\left[\frac{1}{6} - 4\left(\frac{\eta}{R\xi}+\frac{1}{15}\right)\left(\frac{r}{R}\right)^3\right]^2 \sin^2(3\varphi)\,. \tag{33b}$$

The spatial symmetries of the stream function are reflected in the profile of the IEPR (figures 5(b) and (c)). Our prediction of $\dot{\sigma}$ (equation (33)) assume no-slip boundary conditions, and is qualitatively independent of the choice of boundary conditions close to the defect core (i.e. far from the boundary layer). A different choice would only change our prediction quantitatively while preserving the angular symmetries [73]. In appendix F, we demonstrate the existence of an inner region ($r < r_C$) where the IEPR is insensitive to the boundary conditions for all isolated $\pm\frac{1}{2}$ defects.

In short, the local IEPR around isolated defects is spatially inhomogeneous, with symmetries stemming from the vorticity of the backflow around defects: for the $+\frac{1}{2}$ defect, it is mirror-symmetric across the direction of the polarization; for the $-\frac{1}{2}$ defect, it features a six-fold rotational symmetry. The proximity of defects of opposite charges induces perturbations of these profiles. Generally, perturbations of the IEPR profile are more pronounced for $-\frac{1}{2}$ defects. In typical configurations (figure 5(a)), there are no rigorously isolated defects due to the highly correlated distortions of the interfaces across the sample.

The assumption of a constant amplitude of the $Q-$tensor that underlies our derivation leads to quantitative differences between the analytic and the simulated profiles. In simulations, the active force ${f^A}_\alpha \propto \partial_\beta Q_{\alpha\beta}$ (equation (8)) around $\pm\frac{1}{2}$ defects is localized along the interfaces of ϕ, and vanishes at the center of the defects, whereas it is maximal at the center in our analytic solution. The analysis and justification of these discrepancies are deferred to appendix G.

3.3.2. Defect pairs

To predict the profiles of the local IEPR $\dot{\sigma}$ around defect pairs, we construct the director field $\theta_N(\boldsymbol{r})$ by superposing the textures of isolated defects. For a pair of defects with charges (q_1, q_2), the configuration is described by two parameters: the separation d between the defect cores, and the relative angle Φ between the defect orientations. The orientation of the nematic director field (equation (13)) reads

$$\theta_N(x,y) = q_1 \arctan\left(\frac{y\cos\Phi + (x+d/2)\sin\Phi}{(x+d/2)\cos\Phi - y\sin\Phi}\right) + q_2 \arctan\left(\frac{y}{x-d/2}\right). \tag{34}$$

We assume that the scale of the defect cores is small compared to the typical variations of the IEPR profile, and that the amplitude $S = \sqrt{Q_{11}^2 + Q_{12}^2}$ is constant outside the defect cores, so that the variations of $\mathbb{Q}$ are entirely determined by the orientation θ_N. The velocity field $\boldsymbol{v}$ associated with the backflow of the defect pair follows by solving the Stokes equation (equation (7)) by using a Green function: $v_\alpha(\boldsymbol{r}) = \int \mathrm{d}^2\boldsymbol{r}' G_{\alpha\beta}(\boldsymbol{r}-\boldsymbol{r}') f_\beta(\boldsymbol{r}')$ where f is the force acting on the fluid. Using $f_\beta = \partial_\gamma \Sigma_{\beta\gamma}$ we can write:

$$v_\alpha(\boldsymbol{r}) = (\kappa+\zeta)\int \mathrm{d}^2\boldsymbol{r}' G_{\alpha\beta}(\boldsymbol{r}-\boldsymbol{r}')\,\partial_\gamma Q_{\beta\gamma}(\boldsymbol{r}')\,, \tag{35}$$

where the Oseen tensor $\mathbb{G}$ in two dimensions reads [74]:

$$G_{\alpha\beta}(\boldsymbol{r}) = \frac{1}{4\pi\eta}\left[\left(\log\frac{\mathcal{L}}{r} - 1\right)\delta_{\alpha\beta} + \frac{r_\alpha r_\beta}{r^2}\right]. \tag{36}$$

The parameter $\mathcal{L} = R/\sqrt{e}$ is relevant for no-slip boundary conditions. Note that the divergence of $G_{\alpha\beta}$ as $r \to 0$ is consistent with the breakdown of a continuum description near the defects' core.

Finally, the local IEPR follows from substituting the solution for the flow (equation (35)) into equation (18). Below, we examine three cases at a fixed distance ($d = R/2$) when changing the orientation Φ. The orientation of the anisotropic $+\frac{1}{2}$ defects is described by the polarization vector defined as $p_\alpha = -\partial_\beta Q_{\alpha\beta}(\boldsymbol{r} = \boldsymbol{r}_+)$, where $\mathbb{Q}$ is the nematic field (equation (13)) and $\boldsymbol{r}_+$ is the position of the defect core [30]. For all profiles, the local vorticity changes as $\omega \to -\omega$ under the transformation $\Phi \to \Phi + \pi$; given that $\dot{\sigma}$ is quadratic in ω (equation (18)), it is invariant under such a transformation, so we consider only the range $0 \leqslant \Phi \leqslant \pi/2$.

Let us start with a pair of $+\frac{1}{2}$ defects (figure 6(a)). At $\Phi = 0$, the defects have collinear and opposite polarizations that are parallel to the segment that connects the cores; the vortices around each defect interfere negatively, yielding low $\dot{\sigma}$. At $\Phi = \pi/2$, the polarizations are opposite and perpendicular to the connecting segment; the vortices around each defect coalesce into a large vortex, yielding a high $\dot{\sigma}$. In contrast, a $-\frac{1}{2}$ pair does not yield large $\dot{\sigma}$ as we rotate defects (figure 6(b)), since vortices do not coalesce as for a $+\frac{1}{2}$ pair. For a $(+\frac{1}{2}, -\frac{1}{2})$ pair (figure 6(c)), $\dot{\sigma}$ is highest at $\Phi = \pi/2$ as the left vortex of the $+\frac{1}{2}$ does not interfere negatively with the vortices of the $-\frac{1}{2}$ defect. In short, the vortices generated

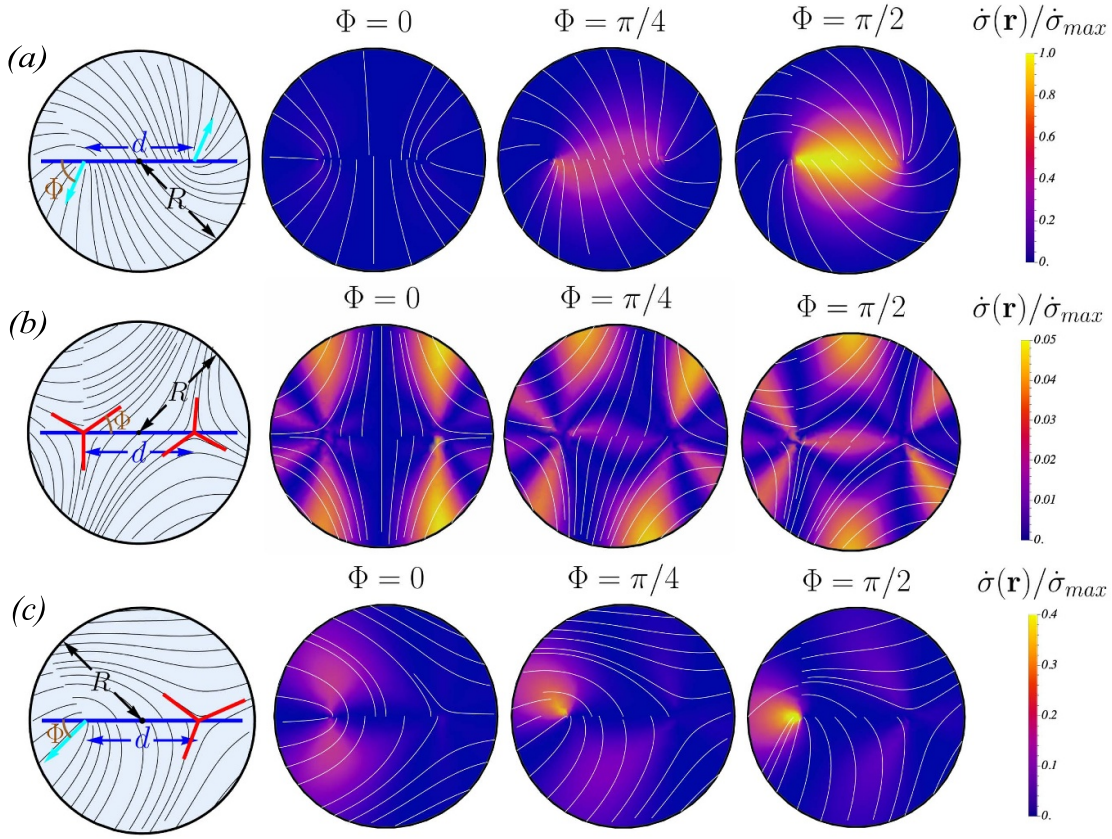

Figure 6. Analytical prediction for the local IEPR $\dot{\sigma}$ (equation (18)): (a) a pair of $+\frac{1}{2}$ defects, (b) a pair of $-\frac{1}{2}$ defects, and (c) a pair of $+\frac{1}{2}$ and $-\frac{1}{2}$ defects. The defects are at a fixed distance d within a disc of radius R, and the angle of orientation changes from $\Phi = 0$ to $\Phi = \pi/2$. The first panel in each row shows the schematic of the configuration. For all panels, the color bars are normalized by the maximum value $\dot{\sigma}_{\max}$ attained for a pair of $+\frac{1}{2}$ defects within the disc.

by the total force regulate the localization of IEPR. Since the total force is localized along the interfaces between regions of small and large ϕ (figure 3(b)), it follows that $\dot{\sigma}$ is also highest at interfaces.

We compare our analytical predictions with some defect pairs spontaneously formed in the turbulent state. For a $+\frac{1}{2}$ pair where $(d, \Phi) \simeq (0.45R, 0.45\pi)$ (figure 5(e)), $\dot{\sigma}$ is higher between defects, in agreement with our predictions (figure 6(a)). For a $(+\frac{1}{2}, -\frac{1}{2})$ pair where $(d, \Phi) \simeq (0.49R, 0.95\pi)$ (figure 5(g)), $\dot{\sigma}$ is higher close to the $+\frac{1}{2}$ defect, and symmetric with respect to its polarization orientation, in agreement with our predictions (figure 6(c)). In both cases, we attribute the slight quantitative deviations to the spatial asymmetries in the numerical solution of the nematic field.

Finally, we consider a symmetric configuration of a $(+\frac{1}{2}, -\frac{1}{2})$ pair (figure 7(a)), and examine the effect of parametrically varying the separation distance d at a fixed orientation $\Phi = 0$. For each value of d, we introduce the integrated IEPR as

$$\dot{\mathcal{S}}_R = \int_{D_R} \dot{\sigma}\,(\boldsymbol{r})\, \mathrm{d}^2\boldsymbol{r}, \tag{37}$$

where D_R is the disc of radius R centered at the mid-point between defect cores. We observe that $\dot{\mathcal{S}}_R$ increases monotonically with d: it vanishes at $d = 0$, and approaches the sum of contributions from isolated defects as d increases, as expected (figure 7(b)). In the turbulent state, the fluid is continuously stirred by the creation and annihilation of $(+\frac{1}{2}, -\frac{1}{2})$ [26]. It is tempting to interpret our symmetric configurations (figure 7(a)) as a time-series of snapshots during such a creation (namely, for increasing d) and annihilation (namely, for decreasing d). Our results suggest that the IEPR increases/decreases monotonically when two defects are brought further/closer infinitely slowly.

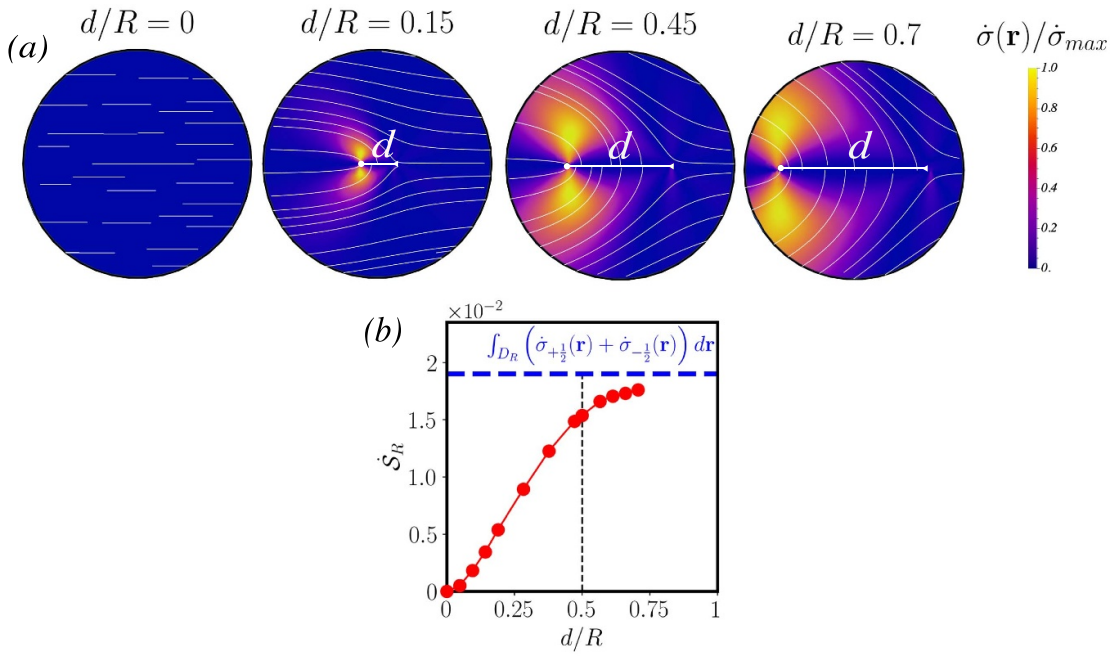

Figure 7. Analytical prediction for the local IEPR $\dot{\sigma}$ (equation (18)) as a function of the distance d between defects within a disc of radius R. (a) Series of snapshots of $\dot{\sigma}$ for various values of d. The colorbars are normalized by the maximum $\dot{\sigma}_{\max}$ attained within the disc. (b) The integrated IEPR $\dot{\mathcal{S}}_R$ (equation (37)) as a function of d/R. The blue dashed line is the sum of the IEPR for the isolated $+\frac{1}{2}$ and $-\frac{1}{2}$ defects in a disc of the same radius R.

4. Discussion

We have examined the relation between the spatial distribution of the IEPR [50] and the location of TDs [26] in active turbulence [5]. Based on a minimal hydrodynamic theory, coupling the density of swimmers and the stream function of the surrounding fluid, we have performed numerical simulations and studied the self-sustained flows that emerge spontaneously despite the absence of inertia. Chaotic (turbulent) flows emerging in active model H were reported in [51]. In this work, we observed two novel flow states in active model H, which we called the laminar and vortex states. This result extends the portfolio of inertia-less turbulence to active model H [51], which goes beyond the well-studied case of active nematics [12].

Using the formalism of stochastic thermodynamics [31, 48, 50], we demonstrate that the dominant contribution to IEPR is generically located in regions of high vorticity. This contribution is due to the coupling between the momentum-conserving fluid (governed by the Stokes equation) and the density of swimmers through active stress. Moreover, using TDs, we have shown that the IEPR represents only a partial estimation of the total dissipation rate. To analyze in detail the spatial profile of IEPR, we build a mapping between the shear stress, which stirs the fluid, and an effective nematic field, by analogy with liquid crystals [12]. Our mapping leads to identifying some $\pm\frac{1}{2}$ defects, with symmetries analogous to that of nematics, defined as locations where the gradient of the swimmer density vanishes. Similarly to active nematics, TDs stir the flow and shape the spatial structure of vortices. Here, we have shown that, remarkably, the vortices near pairs of TDs indicate the dominant contribution to irreversibility. Therefore, our mapping reveals a direct relation between TDs and IEPR.

We provide analytical derivations for the profile of IEPR around $+\frac{1}{2}$ and $-\frac{1}{2}$ defects. Our results predict that the dominant contribution to IEPR stems from configurations where nearby $+\frac{1}{2}$ defects are oriented orthogonally to each other, in direct agreement with numerical simulations. Moreover, we examine the dependence of IEPR on the distance between $(+\frac{1}{2}, -\frac{1}{2})$ pairs, as a first step towards quantifying IEPR during the creation/annihilation of such pairs (a detailed analysis requires resolving the TDs dynamics during creation/annihilation) [75]. We show that the main features of the local IEPR can be predicted analytically by considering point-like idealized TDs, both isolated and paired. Taking into account a finite core size for TDs, we can even predict the finer details of the local IEPR. These results open some unprecedented perspectives for quantifying irreversibility in experimental realizations of active turbulence. Moreover, the strong localization of IEPR in small regions centered around the point-like TDs indicates that the total IEPR across the system may be estimated by a discrete number of local

measurements. It would be interesting to explore further whether the fluctuations of IEPR are also constrained by the TDs statistics [76].

Recently, some protocols have been proposed to control the dynamics of flows and defects in active nematics [77, 78] in line with experiments [79, 80]. From a broader perspective, different control strategies have been put forward to stabilize patterns in various active systems [81–83]. To this end, an important challenge is to identify the relevant degrees of freedom which determine the emerging dynamical patterns. By analyzing how the defect statistics affects the IEPR, we provide the first step towards building protocols which drive the dynamics towards target states at a minimal cost. Our results motivate the search for generic control principles: how local perturbation can result in optimally controlling the dynamics of complex systems [84].

Acknowledgments

It is a pleasure to acknowledge fruitful discussions with Sumesh P Thampi. ÉF acknowledges discussions with Michael E Cates and Rajesh Singh. This research was funded in part by the Grant reference 14389168 (Luxembourg National Research Fund, FNR), and by the Grant No. NSF PHY-2309135 to the Kavli Institute for Theoretical Physics (KITP). B N R acknowledges support from the FNR Grant PRIDE19/14063202/ACTIVE.

Data availability statement

All data that support the findings of this study are included within the article (and any supplementary files).

Supplementary Video available at https://doi.org/10.1088/1367-2630/ae44c3/data1.

Appendix A. Stochastic dynamics of the stream function

To derive the stochastic dynamics of the stream function (equation (10)), we apply the curl operator to the Stokes equation (equation (7)). The term that contains the gradient of pressure vanishes:

$$\nabla \times (\nabla p) = 0, \tag{A.1}$$

and the viscous term gives

$$\nabla \times \left(\eta \nabla^2 \mathbf{v}\right) = -\eta \nabla^4 \psi, \tag{A.2}$$

where $\nabla\times$ is the curl in 2 dimensions and we have used the fact that curl and Laplacian operators commute, and $\partial_y v_x - \partial_x v_y = \nabla^2 \psi$ by definition of the stream function (equation (9)). Defining the force f as

$$f_\alpha = \partial_\beta \left(\Sigma^P_{\alpha\beta} + \Sigma^A_{\alpha\beta}\right) = (\zeta + \kappa)\left[(\delta_{\alpha\beta}/2)\,\partial_\beta \left(\partial_{\gamma\gamma}\phi\right)^2 - \partial_\beta \left(\partial_\alpha \phi \partial_\beta \phi\right)\right], \tag{A.3}$$

where we have used the definitions of $\Sigma^P_{\alpha\beta}$ and $\Sigma^A_{\alpha\beta}$ (equation (6)), we get

$$\begin{aligned} \frac{f_x}{\kappa+\zeta} &= \frac{1}{2}\partial_x \left[\left(\partial_y\phi\right)^2 - \left(\partial_x\phi\right)^2\right] - \partial_y \left[\left(\partial_x\phi\right)\left(\partial_y\phi\right)\right], \\ \frac{f_y}{\kappa+\zeta} &= \frac{1}{2}\partial_y \left[\left(\partial_x\phi\right)^2 - \left(\partial_y\phi\right)^2\right] - \partial_x \left[\left(\partial_x\phi\right)\left(\partial_y\phi\right)\right], \end{aligned} \tag{A.4}$$

from which we deduce

$$\begin{aligned} \frac{\partial_x f_y - \partial_y f_x}{\kappa+\zeta} &= \left(\partial_x\phi\right)\left[-\partial_x\left(\partial^2_{xy}\phi\right) + \partial_y\left(\partial^2_{yy}\phi\right) + 2\partial_x\left(\partial^2_{xy}\phi\right)\right] \\ &\quad + \left(\partial_y\phi\right)\left[-\partial_x\left(\partial^2_{xx}\phi\right) + \partial^2_{yy}\left(\partial_x\phi\right) - 2\partial_x\left(\partial^2_{yy}\phi\right)\right] \\ &= \left(\partial_x\phi\right)\nabla^2\left(\partial_y\phi\right) - \left(\partial_y\phi\right)\nabla^2\left(\partial_x\phi\right). \end{aligned} \tag{A.5}$$

Applying the curl operator $\epsilon_{\alpha\alpha'}\partial_{\alpha'}$ to the noise term $\partial_\beta \Gamma_{\alpha\beta}$, where ϵ is the Levi–Civita matrix ($\epsilon_{xy} = -\epsilon_{yx} = 1$), the noise term $\Xi = \epsilon_{\alpha\alpha'}\partial^2_{\alpha'\beta}\Gamma_{\alpha\beta}$ has Gaussian statistics with zero mean and correlation

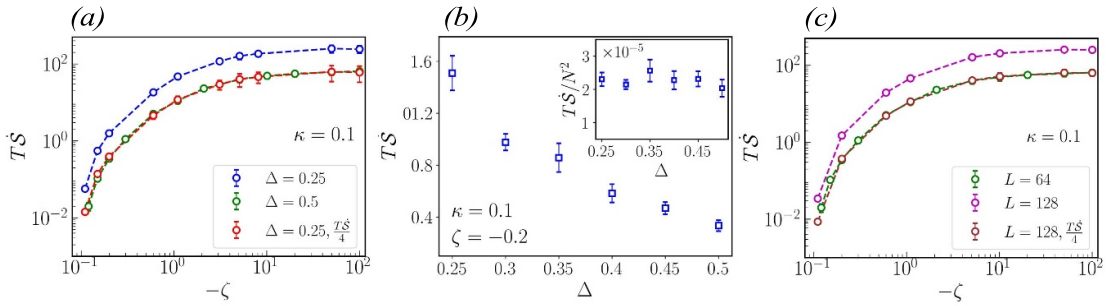

Figure B1. (a) EPR is plotted as a function of activity for various spatial discretizations Δ by fixing L. (b) Variation of EPR with spatial discretizations. The inset plot shows EPR per lattice cell. (c) Plot is same as (a) but by changing L with fixed Δ.

given by

$$\begin{aligned}\langle \Xi(\boldsymbol{r},t)\,\Xi(\boldsymbol{r}',t')\rangle &= \epsilon_{\alpha\alpha'}\epsilon_{\mu\mu'}\left(\delta_{\alpha\mu}\delta_{\beta\nu}+\delta_{\alpha\nu}\delta_{\beta\mu}\right)\partial^4_{\alpha'\beta\mu'\nu}\delta(\boldsymbol{r}-\boldsymbol{r}')\,\delta(t-t')\\ &= \left(\epsilon_{\alpha\alpha'}\epsilon_{\alpha\mu'}\partial^2_{\alpha'\mu'}\nabla^2+\epsilon_{\alpha\alpha'}\epsilon_{\mu\mu'}\partial^4_{\alpha\alpha'\mu\mu'}\right)\delta(\boldsymbol{r}-\boldsymbol{r}')\,\delta(t-t')\\ &= \nabla^4\delta(\boldsymbol{r}-\boldsymbol{r}')\,\delta(t-t'),\end{aligned} \tag{A.6}$$

where we used the identities $\epsilon_{\alpha\alpha'}\epsilon_{\alpha\mu'}=\delta_{\alpha'\mu'}$ and $\epsilon_{\alpha\alpha'}\epsilon_{\mu\mu'}=\delta_{\alpha\mu}\delta_{\alpha'\mu'}-\delta_{\alpha\alpha'}\delta_{\mu\mu'}$. Therefore, combining equations (A.1)–(A.6), we deduce the stream function's dynamics in equation (10).

Appendix B. Numerical methods

To integrate the hydrodynamic equations (equations (1) and (10)), we use a pseudo-spectral numerical scheme. The simulations are performed in a square lattice of size $L\times L$, and the space is discretized as $L=N\Delta$. The grid spacing Δ is kept constant while varying the N to change the system size. The initial condition for ϕ is sampled from randomly in $[-0.1,0.1]$, and ψ is set to zero.

At each time step, the numerical scheme computes the Fourier transform of density $\mathbf{F}[\phi(\boldsymbol{r},t)]=\phi_{\boldsymbol{q}}(t)$ and deduces $\psi_{\boldsymbol{q}}$ as

$$\eta\boldsymbol{q}^4\psi_{\boldsymbol{q}} = (\kappa+\zeta)\,\mathbf{F}\left[(\partial_x\phi)\,\nabla^2(\partial_y\phi)-(\partial_y\phi)\,\nabla^2(\partial_x\phi)\right]+\sqrt{2\eta T}\boldsymbol{q}^2\Lambda_{\psi\boldsymbol{q}}, \tag{B.1}$$

where we have used equation (10). We choose a numerical cut-off on wavenumbers ($q>10^{-8}$) to avoid any divergence at the $q=0$ mode. Aliasing of the Fourier components is prevented by implementing the 2/3 rule [85]. Next, we compute the velocity in real space (equation (9)) from

$$v_x=\mathbf{F}^{-1}\left[\mathrm{i}q_y\psi_{\boldsymbol{q}}\right],\quad v_y=\mathbf{F}^{-1}\left[-\mathrm{i}q_x\psi_{\boldsymbol{q}}\right] \tag{B.2}$$

and the density dynamics (equation (1)) follows in Fourier space as

$$\dot{\phi}_{\boldsymbol{q}} = -\mathbf{F}\left[\boldsymbol{v}\cdot\nabla\phi\right]-aM\boldsymbol{q}^2\phi_{\boldsymbol{q}}+b\mathbf{F}\left[\nabla^2\phi^3\right]-\kappa\boldsymbol{q}^4\phi_{\boldsymbol{q}}-\mathrm{i}\sqrt{2MT}\boldsymbol{q}\cdot\Lambda_{\phi\boldsymbol{q}}. \tag{B.3}$$

In each simulation, the system is allowed to relax and reach a steady state before taking any measurements. To probe finite-size effects, we evaluate the IEPR (equation (18)) for various values of the spacial discretization and the size of the system, showing that our measurements scale like N^2, where N is the number of lattice points, as expected (figure B1).

Appendix C. Nematic director and mean curvature

In this appendix, we summarize the relation between symmetric traceless tensors in 2 dimensions, its principal axes, and the nematic director [63]. Let us consider the most general traceless symmetric tensor $Q_{\alpha\beta}$ in 2 dimensions:

$$Q_{\alpha\beta}=\begin{pmatrix}Q_{11} & Q_{12}\\ Q_{12} & -Q_{11}.\end{pmatrix} \tag{C.1}$$

We interpret $\mathbb{Q}$ as the order parameter of a nematic field, whose orientation is $\theta_N(r,\varphi)$ at every point in space.

C.1. Nematic director

The eigenvalues and eigenvectors of $\mathbb{Q}$ (equation (C.1)) read

$$\lambda_{\pm} = \pm\sqrt{Q_{11}^2 + Q_{12}^2}, \quad \mathbf{v}_{\pm} = \left(\frac{Q_{11} \pm \sqrt{Q_{11}^2 + Q_{12}^2}}{Q_{12}}, 1\right). \tag{C.2}$$

The eigenspace of $Q_{\alpha\beta}$ is defined up to a multiplication of $\mathbf{v}_{\pm}$ by an arbitrary scalar s. We are interested in the direction of the eigenvectors, so we construct the projective space associated with the eigenspace of $Q_{\alpha\beta}$ by identifying $\mathbf{v}_{\pm} \sim s\mathbf{v}_{\pm}$ for any real s. The eigenvectors are orthogonal, so it is sufficient to consider the direction of one of them, say $\mathbf{v}_{+}$ (the direction of $\mathbf{v}_{-}$ is orthogonal to it). In polar form, we get $\mathbf{v}_{+} = |\mathbf{v}_{+}|(\cos\theta_N, \sin\theta_N)$, where the angle θ_N can be deduced from equation (C.2):

$$\tan\theta_N = \frac{(v_+)_y}{(v_+)_x} = \frac{Q_{12}}{Q_{11} + \sqrt{Q_{11}^2 + Q_{12}^2}}. \tag{C.3}$$

Equation (C.3) can be used to compute θ_N if the components $Q_{\alpha\beta}$ are known. Using the trigonometric identity

$$\tan 2\theta_N = \frac{2\tan\theta_N}{1 - \tan^2\theta_N}, \tag{C.4}$$

we find

$$\theta_N = \frac{1}{2}\tan^{-1}\frac{Q_{12}}{Q_{11}}, \tag{C.5}$$

yielding

$$Q_{\alpha\beta} = Q_{11}\begin{pmatrix} 1 & \tan 2\theta_N \\ \tan 2\theta_N & -1 \end{pmatrix} = \frac{Q_{11}}{\cos 2\theta_N}\begin{pmatrix} \cos 2\theta_N & \sin 2\theta_N \\ \sin 2\theta_N & -\cos 2\theta_N. \end{pmatrix} \tag{C.6}$$

Note that the relation $Q_{12} = Q_{11}\tan 2\theta_N$ implies $Q_{11}^2 + Q_{12}^2 = Q_{11}(1 + \tan^2 2\theta_N) = (Q_{11}/\cos 2\theta_N)^2$. The final expression of the nematic tensor is therefore

$$Q_{\alpha\beta} = \sqrt{Q_{11}^2 + Q_{12}^2}\begin{pmatrix} \cos 2\theta_N & \sin 2\theta_N \\ \sin 2\theta_N & -\cos 2\theta_N \end{pmatrix}, \tag{C.7}$$

so $S \equiv \sqrt{Q_{11}^2 + Q_{12}^2}$ is the amplitude of the order parameter. In short, given a symmetric traceless tensor (equation (C.1)), the directions of its principal axes are characterized by the angle $\theta_N(x,y)$ (equation (C.5)) under the identification $\theta_N \sim \theta_N + \pi$.

C.2. Mean curvature

Consider a surface ϕ embedded in $\mathbb{R}^3$. We use the Monge parametrization to represent a point $\mathbf{X} \in \mathbb{R}^3$ on the surface [86]:

$$\mathbf{X}(x,y) = (x, y, \phi(x,y)). \tag{C.8}$$

The tangent vectors $\mathbf{t}_{\alpha}$ ($\alpha = x, y$) and the unit normal to the surface $\mathbf{N}$ are

$$\mathbf{t}_x = (1, 0, \partial_x\phi), \quad \mathbf{t}_y = (0, 1, \partial_y\phi), \quad \mathbf{N} = \frac{(-\partial_x\phi, -\partial_y\phi, 1)}{\sqrt{1 + |\nabla\phi|^2}}. \tag{C.9}$$

The variation of $\mathbf{N}$ between two infinitesimally close points in the surface is parallel to the surface [86], which leads to define the *extrinsic curvature tensor* K_{α}^{β} as

$$\partial_{\alpha}\mathbf{N} = -K_{\alpha}^{\beta}\mathbf{t}_{\beta}, \tag{C.10}$$

where we use summation over repeated indices. The *mean curvature* follows as

$$H = \frac{1}{2}K_{\alpha}^{\alpha}. \tag{C.11}$$

By taking derivatives of $\mathbf{N}$ and projecting onto $\mathbf{t}_\beta$, we construct the tensor K^β_α, and deduce

$$H = \frac{\left(1+\left(\partial_y\phi\right)^2\right)\left(\partial_x\phi\right)^2 - 2\left(\partial_x\phi\right)\left(\partial_y\phi\right)\left(\partial_x\partial_y\phi\right) + \left(1+\left(\partial_x\phi\right)^2\right)\left(\partial_y\phi\right)^2}{2\left(1+|\nabla\phi|^2\right)^{3/2}}, \tag{C.12}$$

where we have used the definition of $\mathbf{N}$ (equation (C.9)).

Appendix D. Derivation of the informatic entropy production rate

To derive the IEPR (equation (17)), we start by writing the path probability for the forward $\mathcal{P}\left(\{\boldsymbol{J},\psi\}_0^t\right)$ and backward $\mathcal{P}^R(\{\boldsymbol{J},\psi\}_0^t)$ paths:

$$\mathcal{P}\left(\{\boldsymbol{J},\psi\}_0^\tau\right) = \exp\left(-\mathcal{A}\right), \quad \mathcal{P}^R\left(\{\boldsymbol{J},\psi\}_0^\tau\right) = \exp\left(-\mathcal{A}^R\right), \tag{D.1}$$

where the $(\mathcal{A},\mathcal{A}^R)$ are the corresponding dynamical actions, and the time-reversal operation is defined by

$$t \to \tau - t, \quad \phi^R(\boldsymbol{r},t) = \phi(\boldsymbol{r},\tau-t), \quad \psi^R(\boldsymbol{r},t) = -\psi(\boldsymbol{r},\tau-t). \tag{D.2}$$

Given that the noise realizations in the dynamics of the density field ϕ (equation (1)) and the stream field ψ (equation (10)) are independent, we separate $(\mathcal{A},\mathcal{A}^R)$ as

$$\mathcal{A} = \int_0^\tau \mathrm{d}t \int \mathrm{d}\boldsymbol{r}\left(\mathcal{A}_\phi + \mathcal{A}_\psi\right), \quad \mathcal{A}^R = \int_0^\tau \mathrm{d}t \int \mathrm{d}\boldsymbol{r}\left(\mathcal{A}^R_\phi + \mathcal{A}^R_\psi\right), \tag{D.3}$$

where $(\mathcal{A}_\phi,\mathcal{A}^R_\phi)$ and $(\mathcal{A}_\psi,\mathcal{A}^R_\psi)$ are the contributions from the dynamics ϕ and ψ, respectively. The IEPR follows as

$$\begin{aligned}\dot{\mathcal{S}} &= \lim_{\tau\to\infty}\frac{1}{\tau}\left(\mathcal{A}^R - \mathcal{A}\right)\\ &= \underbrace{\lim_{\tau\to\infty}\frac{1}{\tau}\int_0^\tau \mathrm{d}t\int \mathrm{d}\boldsymbol{r}\left(\mathcal{A}^R_\phi - \mathcal{A}_\phi\right)}_{\dot{\mathcal{S}}_\phi} + \underbrace{\lim_{\tau\to\infty}\frac{1}{\tau}\int_0^\tau \mathrm{d}t\int \mathrm{d}\boldsymbol{r}\left(\mathcal{A}^R_\psi - \mathcal{A}_\psi\right)}_{\dot{\mathcal{S}}_\psi}.\end{aligned} \tag{D.4}$$

The expression for $\mathcal{A}_\psi$ reads [8]

$$\mathcal{A}_\psi = \frac{1}{4\eta T}\left[\nabla^{-2}\left(L - \eta\nabla^4\psi\right)\right]^2, \quad L = (\kappa+\zeta)\left[\left(\partial_x\phi\right)\nabla^2\left(\partial_y\phi\right) - \left(\partial_y\phi\right)\nabla^2\left(\partial_x\phi\right)\right], \tag{D.5}$$

and $\mathcal{A}_\phi$ is given by

$$\mathcal{A}_\phi = \frac{1}{4MT}\left[\nabla^{-1}\left(\dot{\phi} + \boldsymbol{v}\cdot\nabla\phi + \nabla\cdot\boldsymbol{J}_d\right)\right]^2, \quad \boldsymbol{J}_d = -M\nabla\frac{\delta\mathcal{F}}{\delta\phi}, \tag{D.6}$$

from which we deduce

$$\mathcal{A}^R_\psi = \frac{1}{4\eta T}\left[\nabla^{-2}\left(L + \eta\nabla^4\psi\right)\right]^2, \quad \mathcal{A}^R_\phi = \frac{1}{4MT}\left[\nabla^{-1}\left(\dot{\phi} + \boldsymbol{v}\cdot\nabla\phi - \nabla\cdot\boldsymbol{J}_d\right)\right]^2, \tag{D.7}$$

yielding

$$\dot{\mathcal{S}}_\psi = +\frac{1}{T}\int\langle L\psi\rangle\,\mathrm{d}\boldsymbol{r}, \quad \dot{\mathcal{S}}_\phi = -\frac{1}{T}\int\left\langle\left(\dot{\phi} + \boldsymbol{v}\cdot\nabla\phi\right)\frac{\delta\mathcal{F}}{\delta\phi}\right\rangle\mathrm{d}\boldsymbol{r}, \tag{D.8}$$

where we have used integration by parts. In the expression of $\dot{\mathcal{S}}_\phi$, we identify a vanishing boundary term:

$$\int \mathrm{d}\boldsymbol{r}\left\langle\dot{\phi}\frac{\delta\mathcal{F}}{\delta\phi}\right\rangle = \left\langle\frac{\mathrm{d}\mathcal{F}}{\mathrm{d}t}\right\rangle = \lim_{\tau\to\infty}\frac{\mathcal{F}(\tau)-\mathcal{F}(0)}{\tau} = 0. \tag{D.9}$$

Using the definition $v_\alpha = \epsilon_{\alpha\beta}\partial_\beta\psi$ (equation (9)) and the expression of the free energy $\mathcal{F}$ (equation (3)), the remaining contribution to $\dot{\mathcal{S}}_\phi$ can be written as

$$\begin{aligned} T\dot{\mathcal{S}}_\phi &= -\epsilon_{\alpha\beta}\int \langle (\partial_\beta\psi)\,(\partial_\alpha\phi)\left(dg/d\phi - \kappa\nabla^2\phi\right)\rangle\,\mathrm{d}\boldsymbol{r} \\ &= -\epsilon_{\alpha\beta}\int \langle (\partial_\beta\psi)\left(\partial_\alpha g - \kappa\,(\partial_\alpha\phi)\,\nabla^2\phi\right)\rangle\,\mathrm{d}\boldsymbol{r} \\ &= +\epsilon_{\alpha\beta}\int \langle \psi\left(\partial_\beta\partial_\alpha g - \kappa\partial_\beta\left((\partial_\alpha\phi)\,\nabla^2\phi\right)\right)\rangle\,\mathrm{d}\boldsymbol{r}, \end{aligned} \tag{D.10}$$

where we have integrated by parts. Given that $\epsilon_{\alpha\beta}\partial_\alpha\partial_\beta h(\phi) = 0$ for an arbitrary function h (since $\epsilon_{\alpha\beta} = -\epsilon_{\alpha\beta}$), we deduce

$$T\dot{\mathcal{S}}_\phi = -\kappa\epsilon_{\alpha\beta}\int \langle \psi\,(\partial_\alpha\phi)\,\nabla^2\,(\partial_\beta\phi)\rangle\,\mathrm{d}\boldsymbol{r}. \tag{D.11}$$

Moreover, using the definition of $L = (\kappa+\zeta)\epsilon_{\alpha\beta}(\partial_\alpha\phi)\nabla^2(\partial_\beta\phi)$ (equation (D.5)) and $\dot{\mathcal{S}}_\psi$ (equation (D.8)), we find

$$T\dot{\mathcal{S}}_\psi = +\,(\zeta+\kappa)\,\epsilon_{\alpha\beta}\int \langle \psi\,(\partial_\alpha\phi)\,\nabla^2\,(\partial_\beta\phi)\rangle\,\mathrm{d}\boldsymbol{r}. \tag{D.12}$$

Comparing equations (D.11) and (D.12), we find $\dot{\mathcal{S}}_\phi = -\kappa(\zeta+\kappa)^{-1}\dot{\mathcal{S}}_\psi$, from which we deduce the total IEPR:

$$T\dot{\mathcal{S}} = T\left(\dot{\mathcal{S}}_\phi + \dot{\mathcal{S}}_\psi\right) = \frac{\zeta}{\zeta+\kappa}\int \langle L\psi\rangle\,\mathrm{d}\boldsymbol{r}. \tag{D.13}$$

In the noiseless regime ($T\to 0$), the dynamics of ψ (equation (10)) reduces to $L = \eta\nabla^4\psi$, yielding

$$T\dot{\mathcal{S}} = \frac{\eta\zeta}{\zeta+\kappa}\int \langle\left(\nabla^2\psi\right)^2\rangle\,\mathrm{d}\boldsymbol{r}, \tag{D.14}$$

which coincides with equation (18).

Appendix E. Derivation of the dissipation rate

To derive the relation between the dissipation rate $T\dot{\mathcal{S}}_{\mathrm{tot}}$ (equation (27)) and IEPR $\dot{\mathcal{S}}$ (equation (18)), we start by expressing $T\dot{\mathcal{S}}_{\mathrm{tot}}$ as the sum of products between fluxes and forces [71]:

$$T\dot{\mathcal{S}}_{\mathrm{tot}} = \int (\mathbb{J}\cdot\mathbb{X})\,\mathrm{d}\boldsymbol{r} = \int\left[-J_\alpha\partial_\alpha\frac{\delta\mathcal{F}}{\delta\phi} + v_{\alpha\beta}\left(\Sigma^{\mathrm{tot}}_{\alpha\beta} - \Sigma^{\mathrm{P,tot}}_{\alpha\beta}\right) + r\Delta\mu\right]\mathrm{d}\boldsymbol{r}, \tag{E.1}$$

where we have used the definitions of $(\mathbb{X},\mathbb{J})$ (equation (23)). Integrating by parts the first and second terms in equation (E.1), we deduce

$$\begin{aligned} T\dot{\mathcal{S}}_{\mathrm{tot}} &= \int\left[(\partial_\alpha J_\alpha)\,\frac{\delta\mathcal{F}}{\delta\phi} + v_\beta\left(\partial_\alpha\Sigma^{\mathrm{P,tot}}_{\alpha\beta} - \partial_\alpha\Sigma^{\mathrm{tot}}_{\alpha\beta}\right) + r\Delta\mu\right]\mathrm{d}\boldsymbol{r} \\ &= \int\left[-\frac{\delta\mathcal{F}}{\delta\phi}\,(\partial_t\phi + v_\alpha\partial_\alpha\phi) + v_\beta\partial_\alpha\Sigma^{\mathrm{P,tot}}_{\alpha\beta} + r\Delta\mu\right]\mathrm{d}\boldsymbol{r}, \end{aligned} \tag{E.2}$$

where we have used equations (1) and (21). Using the following identity for the passive stress [69]

$$\phi\,\partial_\alpha\frac{\delta\mathcal{F}}{\delta\phi} = -\partial_\alpha\Sigma^{\mathrm{P,tot}}_{\alpha\beta}, \tag{E.3}$$

together with

$$\int\frac{\delta\mathcal{F}}{\delta\phi}\,\partial_t\phi\,\mathrm{d}\boldsymbol{r} = -\frac{\mathrm{d}\mathcal{F}}{\mathrm{d}t}, \quad \partial_\alpha v_\alpha = 0, \tag{E.4}$$

we then deduce

$$T\dot{\mathcal{S}}_{\mathrm{tot}} = -\frac{\mathrm{d}\mathcal{F}}{\mathrm{d}t} + \int (r\Delta\mu)\,\mathrm{d}\boldsymbol{r}. \tag{E.5}$$

As mentioned in the main text, the term $\mathrm{d}\mathcal{F}/\mathrm{d}t$ vanishes in steady state. Combining the definitions of the chemical rate r (equation (26)) and of the determinant of the Onsager matrix $\det\mathbb{L}$ (equation (25)), we obtain

$$\int (r\Delta\mu)\,\mathrm{d}\boldsymbol{r} = \frac{(2\eta)^4\,\Delta\mu^2}{M}\int (\det\mathbb{L})\,\mathrm{d}\boldsymbol{r} - \int \nu_{\alpha\beta}\Sigma^A_{\alpha\beta}\mathrm{d}\boldsymbol{r}. \tag{E.6}$$

Using the definition $\nu_\alpha = \epsilon_{\alpha\beta}\partial_\beta\psi$ (equation (9)) and integrating by parts, we write the last term in equation (E.6) as follows:

$$\int \nu_{\alpha\beta}\Sigma^A_{\alpha\beta}\mathrm{d}\boldsymbol{r} = \int \epsilon_{\beta\gamma}\partial_\alpha\partial_\gamma\psi\,\Sigma^A_{\alpha\beta}\mathrm{d}\boldsymbol{r} = \int \psi\,\epsilon_{\beta\gamma}\partial_\alpha\partial_\gamma\Sigma^A_{\alpha\beta}\mathrm{d}\boldsymbol{r}. \tag{E.7}$$

Finally, using $\Sigma_{\alpha\beta} = \Sigma^P_{\alpha\beta} + \Sigma^A_{\alpha\beta}$ and equation (6), we can rewrite the dynamics of ψ (equation (10)) in terms of the active stress:

$$\eta\nabla^4\psi = -\epsilon_{\beta\gamma}\frac{\kappa+\zeta}{\zeta}\partial_\alpha\partial_\gamma\Sigma^A_{\alpha\beta}. \tag{E.8}$$

Substituting equation (E.8) into equation (E.7), we find that equation (E.7) is identical to the IEPR of AMH:

$$\int \nu_{\alpha\beta}\Sigma^A_{\alpha\beta}\mathrm{d}\boldsymbol{r} = \frac{\eta\zeta}{\kappa+\zeta}\int \left(\psi\nabla^4\psi\right)\mathrm{d}\boldsymbol{r} = \frac{\eta\zeta}{\kappa+\zeta}\int \left(\nabla^2\psi\right)^2\mathrm{d}\boldsymbol{r} = T\dot{\mathcal{S}}, \tag{E.9}$$

where we have identified the expression of IEPR $\dot{\mathcal{S}}$ (equation (18)). Finally, substituting the relations from equations (E.6) and (E.9) into equation (E.5), we obtain the connection between the steady-state dissipation $T\dot{\mathcal{S}}^{(\mathrm{ss})}_{\mathrm{tot}}$ and $\dot{\mathcal{S}}$ in equation (29). Last, we note that combining the definition of $\det\mathbb{L}$ (equation (25)) with the following relation

$$\tilde{\Sigma}^A_{\alpha\beta}\tilde{\Sigma}^A_{\alpha\beta} = \frac{\zeta^2}{2\Delta\mu^2}|\nabla\phi|^4, \tag{E.10}$$

we can simplify equation (29) as

$$T\left(\dot{\mathcal{S}}^{(\mathrm{ss})}_{\mathrm{tot}} - \dot{\mathcal{S}}\right) = \int \left(c_r\Delta\mu^2 - \frac{\zeta^2}{2\eta}|\nabla\phi|^4\right)\mathrm{d}\boldsymbol{r}. \tag{E.11}$$

Therefore, any local inhomogeneity of the swimmer density ϕ tends to reduce $\dot{\mathcal{S}}^{(\mathrm{ss})}_{\mathrm{tot}} - \dot{\mathcal{S}}$.

Appendix F. Independence of IEPR from boundary conditions

In this appendix, we demonstrate that close to the defect the profile of IEPR (equation (33)) does not depend on the specific boundary condition. In fact, this result stems from the fact that the effects of boundary conditions decay within a boundary layer of thickness δ. We start from the stream function of a $+\frac{1}{2}$ defect: $\psi = \bar{\psi}_{+\frac{1}{2}} + \psi_0$ (section 3.3.1), with $\bar{\psi}_{+\frac{1}{2}}$ given by equation (32*a*) and $\psi_0 = (a_1 r + b_1 r^3)\sin\varphi$. We impose a constant velocity at $r = R$ directed along the $x-$axis:

$$v_x(R,\varphi) = v_R, \quad v_y(R,\varphi) = -\partial_x\psi(R,\varphi) = 0, \tag{F.1}$$

where $v_x(r,\varphi) = \partial_y\psi(r,\varphi)$ and $v_y(r,\varphi) = -\partial_x\psi(r,\varphi)$ can be calculated easily [73]:

$$v_x(r,\varphi) = a_1 + b_1 r^2(2-\cos 2\varphi) + \frac{\zeta}{12\eta}\left[3(R-r) + r\cos 2\varphi\right], \tag{F.2}$$

$$v_y(r,\varphi) = -b_1 r^2\sin 2\varphi + \frac{\zeta}{12\eta}r\sin 2\varphi. \tag{F.3}$$

Substituting equation (F.2) into equation (F.1), we determine the two coefficients (a_1, b_1):

$$a_1 = v_R - \frac{\zeta R}{6\eta}, \quad b_1 = \frac{\zeta}{12R\eta}. \tag{F.4}$$

Correspondingly, the stream function satisfying the boundary conditions is

$$\psi_{+\frac{1}{2}} = \left(v_R + \frac{\zeta}{12R\eta}(r-R)^2\right)r\sin\varphi. \tag{F.5}$$

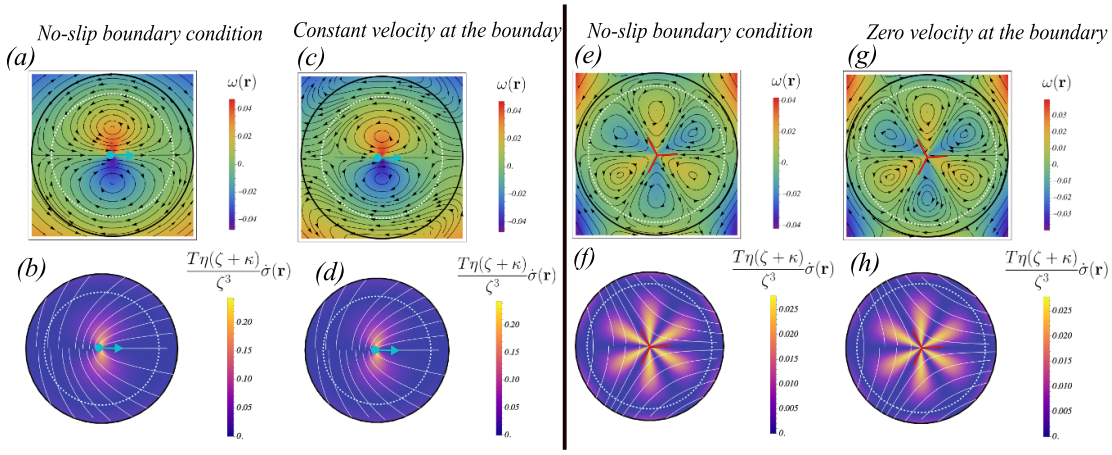

Figure F1. Analytical prediction for the local IEPR and velocity fields around isolated defects topological: for a $+\frac{1}{2}$ defect, (a) and (b) no-slip boundary and (c)–(d) constant-velocity boundary; for a $-\frac{1}{2}$ (e)–(f) no-slip boundary and (g)–(h) constant-velocity boundary. Parameters: $\kappa = 0.1$, $\zeta = 0.16$, $\eta = 1.67$, and $\xi \gg R$ (no-slip limit). The white dashed circles indicate the inner region $r < r_C$ wherein results are expected to be universal and insensitive to the boundary conditions.

Substituting equation (F.5) into equation (19), we find that the IEPR is independent of v_R, since $\nabla^2(r\sin\varphi) = 0$:

$$T\dot{\sigma}_{+\frac{1}{2}}(\boldsymbol{r}) = \frac{\zeta^3}{\eta(\kappa+\zeta)}\left[\frac{1}{2} - \frac{2}{3}\frac{r}{R}\right]^2 \sin^2\varphi\,. \tag{F.6}$$

We note that the differences between equations (F.6) and (33) should be localized in a boundary layer of thickness δ. We expect that, in the bulk ($r < r_C \simeq R - \delta$), the solution is only mildly dependent on the specific boundary conditions. We estimate r_C as the radius where the IEPR is minimum. Imposing $\partial_r\dot{\sigma}_{+\frac{1}{2}}(r_C, \varphi) = 0$ on equation (F.6), we find $r_C = 3R/4$. Figures F1(a) and (c) [resp. (b,d)] compare the vorticity [resp. the IEPR] of an isolated $+\frac{1}{2}$ defect. The dashed white circle indicates $r = r_C$. While the solutions are different at $r = R$ (black circle), they are almost identical in the bulk ($r < r_C$) thus supporting the claim that IEPR has a universal profile close to the defects' center.

Following the same procedure and imposing $v_R = 0$ (equation (F.1)) on the velocity of a $-\frac{1}{2}$ defect, we find the following expressions for the constants:

$$a_1 = \frac{7R\alpha}{240\eta R^2}, \quad b_1 = -\frac{R\alpha}{60\eta R^4}. \tag{F.7}$$

The corresponding expression of the IEPR is

$$T\dot{\sigma}_{-\frac{1}{2}}(\boldsymbol{r}) = \frac{\zeta^3}{\eta(\kappa+\zeta)}\left[\frac{1}{6} - \frac{5}{15}\left(\frac{r}{R}\right)^3\right]^2 \sin^2(3\varphi)\,. \tag{F.8}$$

The comparison between equation (33*b*) (no-slip BCs) and equation (F.8) is shown in figures F1(f) and (h), respectively. The panels figures F1(e) and (g) show the corresponding vorticity and flow fields. Similarly to the case of the $+\frac{1}{2}$ defect, the solutions are almost identical within a radius $r_C = 5^{1/3}R/2$, as determined by imposing $\partial_r\dot{\sigma}_{-\frac{1}{2}}(r_C, \varphi) = 0$.

Appendix G. Spatial distribution of the active force

In this appendix, we comment on the relation between the local IEPR $\dot{\sigma}$ (equation (19)) and the distribution of the total force $f_\alpha \propto \partial_\beta Q_{\alpha\beta}$ (equation (8)) around *individual* defects by comparing numerical simulations with some analytical profiles. In the turbulent state, we consider a specific region with a $+\frac{1}{2}$ defect, whose orientation is indicated with a green arrow (figure G1(a)). The corresponding IEPR is maximal on the two sides of the defect (figure G1(b)), is approximately symmetric with respect to reflections across the defect's orientation, and is comparatively lower near the origin. In what follows, we provide some arguments to reproduce the profiles of $\dot{\sigma}$ and f_α around the defect.

In section 3.3.1, our analytic profile of the local IEPR $\dot{\sigma}$ around a point-like defect (equation (33*a*)) assumes that the defect is isolated and the core size is zero, namely the amplitude of the $Q-$tensor is

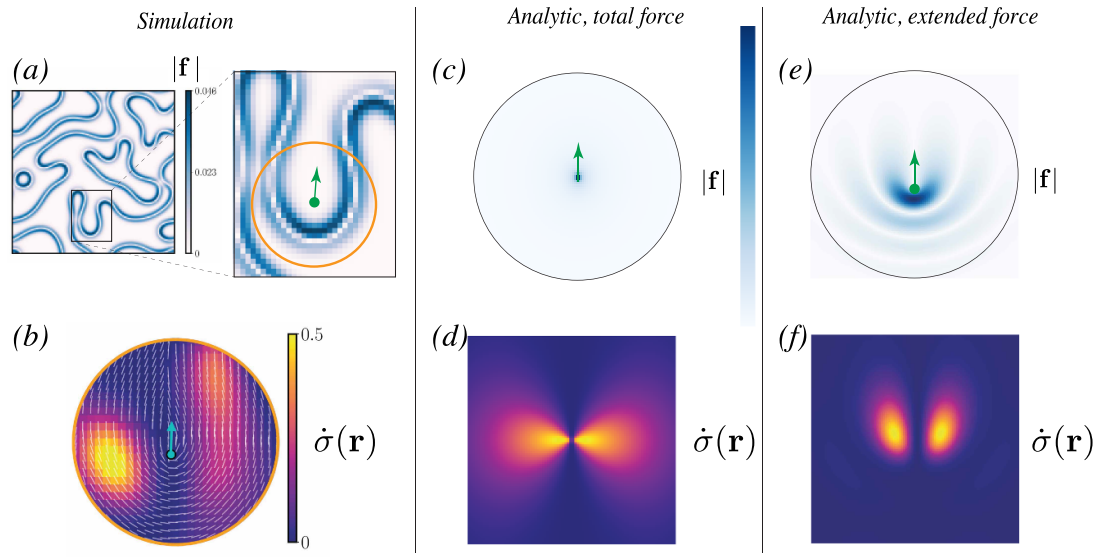

Figure G1. Prediction of the qualitative localization of the IEPR derived from various force fields. The plots are in arbitrary units. (a), (b) Exact force field and corresponding IEPR form numerical simulations. Panel (c): Analytic force field around an isolated $+\frac{1}{2}$ defect (analog to active nematics, [73]). Note that the force is maximal at the center of the defect, contrary to (a). Consequently, while the mirror symmetry is qualitatively preserved, the IEPR (Panel (d)) is maximal at the center, and there is no separation between the two lobes of IEPR. Panel (e): Analytic ansatz for the force field around a $+\frac{1}{2}$ defect, which qualitatively reproduces the symmetries of (Panel (a), inset) as well as the localization along the interface. The corresponding IEPR (Panel (f)) has two localized lobes consistent with the full solution shown in Panel (b).

constant everywhere except at the origin (appendix C). As a result, the corresponding force profile $|\mathbf{f}|$ is strongly localized at the defect core (figure G1(c)), and $\dot{\sigma}$ is maximal at the defect core with a mirror symmetry with respect to the defect orientation (figure G1(d)), in contrast with the numerical profiles (figures G1(a) and (b)).

We now show that the lobed-structure of figures G1(a) and (b) is related to the non-constant amplitude of the $Q-$tensor close to the defect core. We propose an ansatz for the force field $\hat{\mathbf{f}}(\mathbf{r})$ that qualitatively mimics the geometry of the numerical profile:

$$\hat{\mathbf{f}}(\mathbf{r}) = \mathrm{e}^{-r}\nabla\chi(\mathbf{r}), \quad \chi = \frac{1}{2}\left[1-\cos\left(2r\cos\frac{\theta}{2}\right)\right], \tag{G.1}$$

where we assume that the defect is at the origin of the coordinate system, $r=\sqrt{x^2+y^2}$, and $\theta = \arctan(y/x)$. The ansatz in equation (G.1) is localized along the interface, vanishes at the defect core, and has a mirror symmetry (figure G1(e)), as seen in the numerical solution (figure G1(a)). The corresponding IEPR profile follow by using equations (19) and (35): it features two well-separated lobes located symmetrically with respect to the defect orientation (figure G1(f)) in agreement with simulations (figure G1(b)).

In short, we have shown that, for an individual defect, the geometry of the IEPR profile $\dot{\sigma}$ is encoded in the details of the corresponding force profile $|\mathbf{f}|$ close to the defect core. For defect pairs (section 3.3.2), the deviation between our analytics (that rely on point-defect assumption) and numerics is less severe (figures 5(d)–(g)). In this case, the constructive interference of vorticities occurs along the line connecting the two defects centers: the profile $\dot{\sigma}$ is overwhelmingly dominated by these vorices, so the details close to defect core are largely irrevelant.

ORCID iDs

Francesco Serafin 0000-0001-8924-0665
Étienne Fodor 0000-0003-1372-2195

References

[1] Marchetti M C, Joanny J F, Ramaswamy S, Liverpool T B, Prost J, Rao M and Simha R A 2013 *Rev. Mod. Phys.* **85** 1143–89
[2] Fodor E and Marchetti M C 2018 *Physica A* **504** 106–20
[3] Chaté H 2020 *Annu. Rev. Condens. Matter Phys.* **11** 189–212

[4] Cates M E and Tailleur J 2015 *Annu. Rev. Condens. Matter Phys.* **6** 219–44
[5] Alert R, Casademunt J and Joanny J F 2022 *Annu. Rev. Condens. Matter Phys.* **13** 143–70
[6] Hohenberg P C and Halperin B I 1977 *Rev. Mod. Phys.* **49** 435–79
[7] Wittkowski R, Tiribocchi A, Stenhammar J, Allen R J, Marenduzzo D and Cates M E 2014 *Nat. Commun.* **5** 4351
[8] Nardini C, Fodor E, Tjhung E, van Wijland F, Tailleur J and Cates M E 2017 *Phys. Rev. X* **7** 021007
[9] Markovich T, Fodor E, Tjhung E and Cates M E 2021 *Phys. Rev. X* **11** 021057
[10] Doostmohammadi A, Ignés-Mullol J, Yeomans J M and Sagués F 2018 *Nat. Commun.* **9** 3246
[11] Martínez-Prat B, Alert R, Meng F, Ignés-Mullol J, Joanny J F, Casademunt J, Golestanian R and Sagués F 2021 *Phys. Rev. X* **11** 031065
[12] Alert R, Joanny J F and Casademunt J 2020 *Nat. Phys.* **16** 682–8
[13] Dombrowski C, Cisneros L, Chatkaew S, Goldstein R E and Kessler J O 2004 *Phys. Rev. Lett.* **93** 098103
[14] Wensink H H, Dunkel J, Heidenreich S, Drescher K, Goldstein R E, Löwen H and Yeomans J M 2012 *Proc. Natl Acad. Sci. USA* **109** 14308–13
[15] Dunkel J, Heidenreich S, Drescher K, Wensink H H, Bär M and Goldstein R E 2013 *Phys. Rev. Lett.* **110** 228102
[16] Patteson A E, Gopinath A and Arratia P E 2018 *Nat. Commun.* **9** 5373
[17] Liu Z, Zeng W, Ma X and Cheng X 2021 *Soft Matter* **17** 10806–17
[18] Creppy A, Praud O, Druart X, Kohnke P L and Plouraboué F 2015 *Phys. Rev. E* **92** 032722
[19] Sanchez T, Chen D T N, DeCamp S J, Heymann M and Dogic Z 2012 *Nature* **491** 431–4
[20] Guillamat P, Ignés-Mullol J and Sagués F 2017 *Nat. Commun.* **8** 564
[21] Lemma L M, DeCamp S J, You Z, Giomi L and Dogic Z 2019 *Soft Matter* **15** 3264–72
[22] Tan A J, Roberts E, Smith S A, Olvera U A, Arteaga J, Fortini S, Mitchell K A and Hirst L S 2019 *Nat. Phys.* **15** 1033–9
[23] Doostmohammadi A, Thampi S P, Saw T B, Lim C T, Ladoux B and Yeomans J M 2015 *Soft Matter* **11** 7328–36
[24] Blanch-Mercader C, Yashunsky V, Garcia S, Duclos G, Giomi L and Silberzan P 2018 *Phys. Rev. Lett.* **120** 208101
[25] Lin S Z, Zhang W Y, Bi D, Li B and Feng X Q 2021 *Commun. Phys.* **4** 21
[26] Giomi L, Bowick M J, Ma X and Marchetti M C 2013 *Phys. Rev. Lett.* **110** 228101
[27] Thampi S P, Golestanian R and Yeomans J M 2013 *Phys. Rev. Lett.* **111** 118101
[28] Giomi L 2015 *Phys. Rev. X* **5** 031003
[29] Shankar S, Ramaswamy S, Marchetti M C and Bowick M J 2018 *Phys. Rev. Lett.* **121** 108002
[30] Shankar S and Marchetti M C 2019 *Phys. Rev. X* **9** 041047
[31] Lebowitz J L and Spohn H 1999 *J. Stat. Phys.* **95** 333–65
[32] Maes C 1999 *J. Stat. Phys.* **95** 367–92
[33] Kurchan J 1998 *J. Phys. A* **31** 3719
[34] Onsager L 1931 *Phys. Rev.* **37** 405–26
[35] Fodor E, Nardini C, Cates M E, Tailleur J, Visco P and van Wijland F 2016 *Phys. Rev. Lett.* **117** 038103
[36] Borthne O L, Fodor E and Cates M E 2020 *New J. Phys.* **22** 123012
[37] Martin D, O'Byrne J, Cates M E, Fodor E, Nardini C, Tailleur J and van Wijland F 2021 *Phys. Rev. E* **103** 032607
[38] Suchanek T, Kroy K and Loos S A M 2023 *Phys. Rev. Lett.* **131** 258302
[39] Alston H, Cocconi L and Bertrand T 2023 *Phys. Rev. Lett.* **131** 258301
[40] Agranov T, Jack R L, Cates M E and Fodor E 2024 *New J. Phys.* **26** 063006
[41] Agranov T, Jack R L, Cates M E and Fodor E 2025 *New J. Phys.* **27** 104602
[42] Proesmans K, Falasco G, Mohite A T, Esposito M and Fodor E 2025 *Phys. Rev. E* **112** 024103
[43] Gaspard P and Kapral R 2019 *Adv. Phys. X* **4** 1602480
[44] Aslyamov T, Avanzini F, Fodor E and Esposito M 2023 *Phys. Rev. Lett.* **131** 138301
[45] Bebon R, Robinson J F and Speck T 2025 *Phys. Rev. X* **15** 021050
[46] Chatzittofi M, Agudo-Canalejo J and Golestanian R 2024 *Phys. Rev. Res.* **6** L022044
[47] Cocconi L, Chatzittofi M and Golestanian R 2025 *Phys. Rev. Res.* **7** L042062
[48] Seifert U 2012 *Rep. Prog. Phys.* **75** 126001
[49] Peliti L and Pigolotti S 2021 *Stochastic Thermodynamics: An Introduction* (Princeton University Press)
[50] Fodor E, Jack R L and Cates M E 2022 *Annu. Rev. Condens. Matter Phys.* **13** 215–38
[51] Tiribocchi A, Wittkowski R, Marenduzzo D and Cates M E 2015 *Phys. Rev. Lett.* **115** 188302
[52] Singh R and Cates M E 2019 *Phys. Rev. Lett.* **123** 148005
[53] Das A, Bhattacharjee J K and Kirkpatrick T R 2020 *Phys. Rev. E* **101** 023103
[54] Bhattacharjee J K and Kirkpatrick T R 2022 *Phys. Rev. Fluids* **7** 034602
[55] Padhan N B, Kiran K V and Pandit R 2024 *Soft Matter* **20** 3620–7
[56] Bray A 1994 *Adv. Phys.* **43** 357–459
[57] Stenhammar J, Tiribocchi A, Allen R J, Marenduzzo D and Cates M E 2013 *Phys. Rev. Lett.* **111** 145702
[58] Bixon M and Zwanzig R 1969 *Phys. Rev.* **187** 267–72
[59] Chaikin P M and Lubensky T C 1995 *Principles of Condensed Matter Physics* (Cambridge University Press)
[60] Ibrahimi M and Merkel M 2023 *New J. Phys.* **25** 013022
[61] Ibrahimi M and Merkel M 2025 *PRX Life* **3** 043013
[62] Gsell S, Tlili S, Merkel M and Lenne P F 2025 *Nat. Phys.* **21** 644–53
[63] Gennes P G D and Prost J 1993 *The Physics of Liquid Crystals* (Oxford University Press)
[64] Janssen H 1976 *Z. Phys. B* **23** 377–80
[65] Martin P C, Siggia E D and Rose H A 1973 *Phys. Rev. A* **8** 423–37
[66] Onsager L and Machlup S 1953 *Phys. Rev.* **91** 1505–12
[67] Landau L D and Lifshitz L M 1987 *Fluid Mechanics: Course of Theoretical Physics* vol 6 (Elsevier Pergamon)
[68] Qu Z, Schildknecht D, Shadkhoo S, Amaya E, Jiang J, Lee H J, Larios D, Yang F, Phillips R and Thomson M 2021 *Commun. Phys.* **4** 198
[69] Cates M E and Nardini C 2025 *Rep. Prog. Phys.* **88** 056601
[70] Kruse K, Joanny J F, Jülicher F, Prost J and Sekimoto K 2004 *Phys. Rev. Lett.* **92** 078101
[71] Groot S R D and Mazur P 1962 *Non-Equilibrium Thermodynamics* (North-Holland)
[72] Esposito M 2012 *Phys. Rev. E* **85** 041125
[73] Giomi L, Bowick M J, Mishra P, Sknepnek R and Marchetti M C 2014 *Phil. Trans. R. Soc. A* **372** 20130365

[74] Di Leonardo R, Keen S, Ianni F, Leach J, Padgett M J and Ruocco G 2008 *Phys. Rev. E* **78** 031406
[75] Yashunsky V, Beer A, Neimand E, Pearce D, Corbett D and Ariel G 2025 Irreversibility and symmetry breaking in the creation and annihilation of defects in active living matter (*Preprint Research Square*)
[76] Mahault B, Tang E and Golestanian R 2022 *Nat. Commun.* **13** 3036
[77] Shankar S, Scharrer L V, Bowick M J and Marchetti M C 2024 *Proc. Natl Acad. Sci. USA* **121** e2400933121
[78] Ghosh S, Baskaran A and Hagan M F 2025 *J. Chem. Phys.* **162** 134902
[79] Zhang R *et al* 2021 *Nat. Mater.* **20** 875–82
[80] Nishiyama K, Berezney J, Norton M M, Aggarwal A, Ghosh S, Zarei Z, Hagan M F, Fraden S and Dogic Z 2025 *Phys. Rev. X* **15** 041053
[81] Shankar S, Souslov A, Bowick M J, Marchetti M C and Vitelli V 2022 *Nat. Rev. Phys.* **4** 380–98
[82] Davis L K, Proesmans K and Fodor E 2024 *Phys. Rev. X* **14** 011012
[83] Alvarado J, Teich E G, Sivak D A and Bechhoefer J 2026 *Annu. Rev. Condens. Matter Phys.* **17** 1947–5454
[84] Fodor E 2024 *Europhys. News* **55** 20–23
[85] Canuto C, Hussaini M Y, Quarteroni A M and Zang T A 2010 *Spectral Methods: Fundamentals in Single Domains* (Springer)
[86] do Carmo M P 1994 *Differential Geometry of Surfaces* (Springer)